Nano-Petrophysical Properties of the Bone Spring and the Wolfcamp Formation in the Delaware Basin, New Mexico, USA.

By: Ashley Chang

Presented to the Faculty of the Graduate School of

The University of Texas at Arlington in Partial Fulfillment

of the Requirements for the Degree of

MASTER OF SCIENCE IN EARTH AND ENVIROMENTAL SCIENCES

THE UNIVERSITY OF TEXAS AT ARLINGTON

MAY 2019

Acknowledgements

I would like to thank my thesis advisor Dr. Qinhong Hu. His knowledge and passion for this field is truly aspiring. I would also like to thank the thesis committee members, Dr. John Wickham and Dr. Majie Fan for providing me with insight and guidance throughout my time at UTA.

Thanks also goes to Annabelle Lopez from the New Mexico Bureau of Geology & Mineral Resources (NMBGR) for providing me with the samples to make this research possible. The numerous core samples and geologic data that were provided to me has been extremely beneficial for my research. Drilling Info is also thanked for the complimentary subscription extended to Dr. Hu's research group.

I would like to thank Qiming Wang for the numerous times he has helped me along the way. I wish nothing but the best for Qiming and his future endeavors. Furthermore, I would like to thank Nabil, my family, and friends for their constant support and motivation. Their love has allowed me to be who I am today, and I am truly grateful to have people who mean so much to me in my life.

April 16, 2019

Abstract

Nano-Petrophysical Properties of the Bone Spring and the Wolfcamp Formation in the Delaware Basin, New Mexico, USA.

Ashley Chang, MS

The University of Texas at Arlington, 2019

Supervising Professor: Qinhong Hu

The Permian Basin is one of the largest oil producing basins in the United States. The Permian Basin is 260 miles by 300 miles in area and encompasses 52 counties in southeast New Mexico and West Texas. In the past decade, the Permian Basin has exceeded its previous peak from the early 1970s (EIA, 2018). Now, the basin has generated more than 33.4 billion barrels of oil and roughly 118 trillion cubic feet of natural gas (EIA, 2018). The Permian Basin is a very complex sedimentary system, with three main sub-divisions that are geologically and stratigraphically different from one another. These three sub-divisions are the Midland Basin, Central Basin Platform and the Delaware Basin. The Delaware Basin, specifically the Bone Spring and Wolfcamp Formations, will be the focus of this study.

Although the production in the Permian Basin has been accelerating, the steep decline rate in the production of the basin is a realistic concern. To better understand the factors contributing to the production decline rate, this study will investigate the pore structure and fluid migration within the Bone Spring and Wolfcamp Formations. Seven samples from the Wolfcamp

Formation are studied, along with two samples from the First Bone Spring unit and one sample from the Second Bone Spring unit. The methods used in this investigation include: total organic carbon (TOC) analysis and pyrolysis for the geochemistry, x-ray diffraction (XRD) to determine the mineralogy, vacuum saturation and liquid displacement, mercury intrusion capillary pressure (MICP) measurements of the sample's petrophysical properties (such as porosity, pore size distribution, tortuosity and permeability), and spontaneous imbibition to determine the pore connectivity in DI water and DT2 (n-decane: toluene= 2:1 in volume) fluids.

The results from the methods stated above show that samples from the Wolfcamp and Bone Spring Formations are quartz or carbonate rich and have TOC values that range from 0.08-1.96%. The porosity of all samples range between 0.36-7.65%. Most samples have pores that are in the micro-fracture and intergranular pore range (>100 nm), with only three samples falling within the intragranular, organic matter, and inter-clay platelet pore range (2.5-50 nm). The samples with a predominant pore-throat network interval of 2.8-50 nm have a permeability that ranges from 0.55 nD to 294 nD, and a geometrical tortuosity that ranges from 2.7-85.2. Samples that have a predominant pore-throat network of >100 nm have a range of 2.55×10^4 nD to 6.02×10^9 nD in permeability, and a geometrical tortuosity range of 0.2-5.3. Three out of the 10 samples display a good pore connectivity towards DT2 fluid, and all samples show poor pore connectivity with DI water.

Table of Contents

List of Illustrations

List of Tables

Chapter 1

Introduction

The Permian Basin is one of the major tight oil and shale gas plays in the United States. This basin extends over 250 miles in width and over 300 miles in length. The Midland and Delaware Basin of the Permian Basin are vital players in the oil and gas industry. Drilling in the Permian Basin begin in the 1920s. Production within the basin began to rise from the use of horizontal drilling and hydraulic fracturing about 10+ years ago. This basin has generated more than 33.4 billion barrels of oil and roughly 118 trillion cubic feet of natural gas as of September 2018 (EIA, 2018). In November 2018, the U.S. Department of Interior announced that the Bone Spring Formation and underlying Wolfcamp Shale in the Delaware Basin contains an estimated mean of 46.3 billion barrels of oil, 281 trillion cubic feet of natural gas, and 20 billion barrels of natural gas liquids (USGS, 2018). The USGS assessment of the Delaware Basin is more than two times larger than the assessment made in 2016 of the Midland Basin (USGS, 2018).

As the Permian Basin is amid a boom, the potential issue of maturing wells falling short of production projections is becoming a realistic concern. A study by Wood Mackenzie Ltd. found that Wolfcamp shale wells that were 60% for the 1st year of production, still lingers at a decline rate of 12-14% per year after five years, which is much higher than the annual average of 5-10% in most unconventional reservoirs (Wood Mackenzie Ltd., 2018). Figure 1 shows the average decline profile of Midland Wolfcamp Deep Basin tight oil wells, as well as the distribution of Midland Wolfcamp Deep Basin decline after five years of production. The trends presented in Figure 1 holds true for most Wolfcamp sub-plays in both the Midland and Delaware Basins, as well as the Bone Spring play (Wood Mackenzie Ltd., 2018).

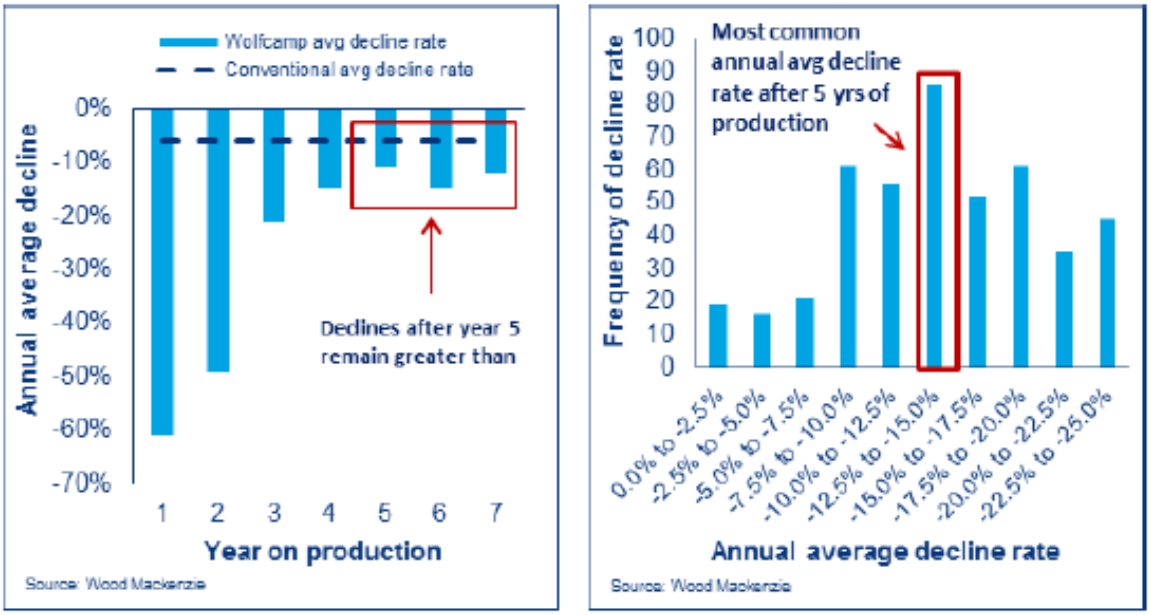

Figure 1: The annual average decline profile (left) and distribution after five years of production (right) of Midland Wolfcamp Deep Basin tight oil wells (Wood Mackenzie Ltd., 2018).

The potential decline rate is a concern, but the research into the contributing factors connected to this decline are very rare. This study will investigate if the pore structure and fluid migration through the pores will provide a better understanding to the contributing factors of the decline rate in the Permian Basin.

Chapter 2

Geologic Setting

The Permian Basin is an asymmetrical, northwest to southeast-trending sedimentary system in West Texas and Southeast New Mexico. The Permian Basin has a surface area that is more than 75,000 sq. miles and includes 52 counties from West Texas and Southeast New Mexico (EIA, 2018). The Marathon-Ouachita Fold Belt bounds the basin to the south, and the west is bound by the Diablo Platform (EIA, 2018). The north side of the basin is bound by the Matador Arch, and the east side is bound by the Eastern shelf (EIA, 2018). The Permian Basin comprises several component basins, with three main sub-divisions as the Midland Basin, Central Basin Platform, and the Delaware Basin. Figure 2.1 shows the three main sub-divisions within the Permian Basin and the structural and tectonic features present within the area.

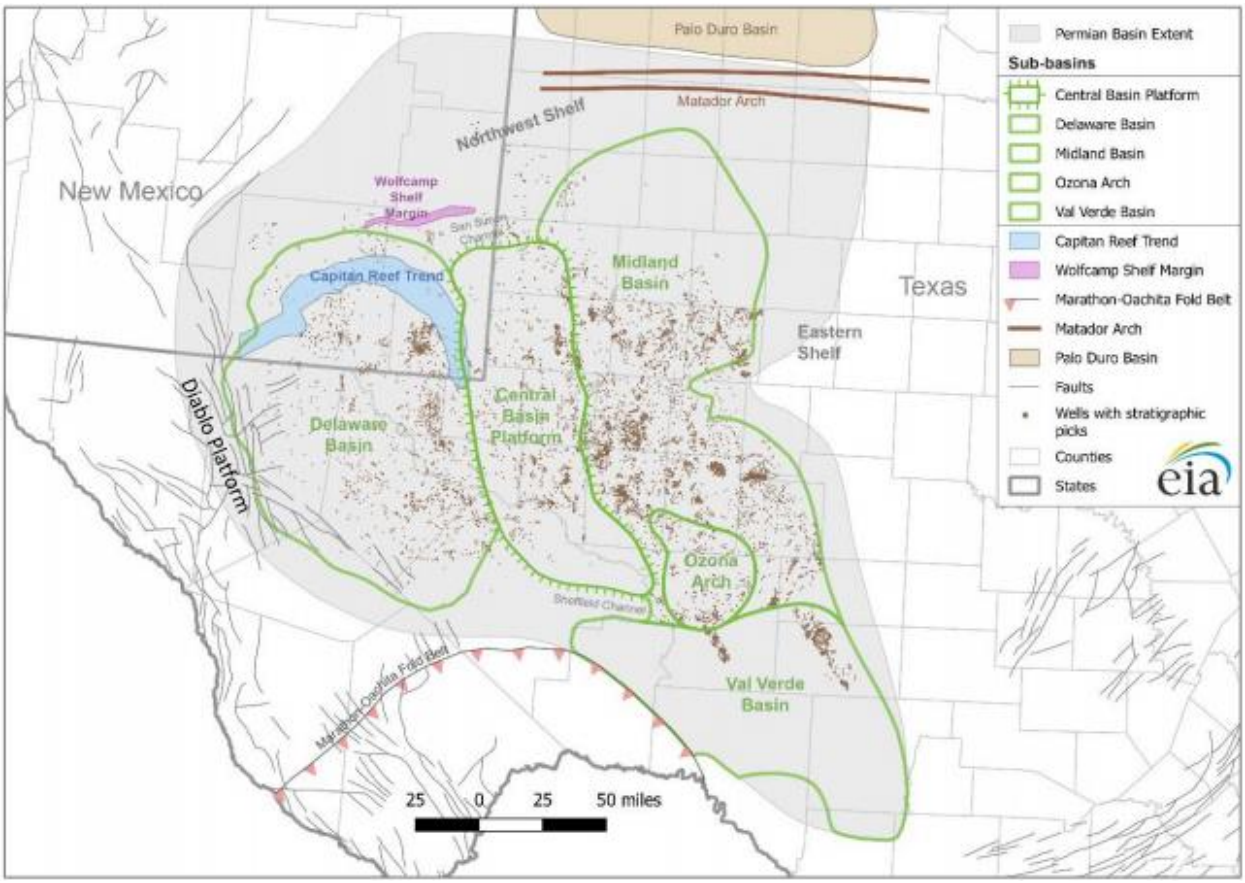

Figure 2.1: The structural and tectonic features of the Permian Basin (EIA, 2018).

The Permian Basin began its formation in late Mississippian and early Pennsylvanian. The region in which the Permian basin formed is an open marine area known as the Tobosa Basin (Sutton, 2014). The Tobosa Basin formed in the Precambrian basement of the North American plate by an asymmetric structural flexure (EIA, 2018). A massive amount of clastic sediments were deposited into the basin during the Cambrian to Mississippian period during phases of basin development (EIA, 2018). The deposition of these sediments in the Tobosa Basin formed a depression (Sutton, 2014). Tectonic activity began in the Mississippian and early Pennsylvanian (Sutton, 2014). This tectonic activity was a result of the formation of Pangea from the collision of the supercontinents Laurasia and Gondwana (Sutton, 2014). Episodes of faulting, uplift, erosion and varying subsidence resulted in the deformation of the Tobosa Basin, resulting in the division of the province into sub-basins (Keller et al., 1980). The two sub-basins are the Delaware Basin on the west and the Midland Basin on the east (Keller et al., 1980). As the Midland and Delaware Basins were forming, broad limestone shelves began to grow around them (Keller et al., 1980). The limestones covered the shelves and eroded roots of the central mountains forming the Central Basin Platform (Keller et al., 1980). Along the Delaware Basin, a vertical movement continued, rapidly deepening the basin and similarly deepening the Midland Basin on a smaller scale (Keller et al., 1980). Due to a rapid subsidence in the Midland and Delaware Basins and the uplift of the Central Basin Platform, the main phase of basin differentiation took place during the Pennsylvanian and Wolfcampian time (EIA, 2018). During the late Pennsylvanian time, there was an active fault zone along the perimeter of the Central Basin platform (EIA, 2018). The Strawn carbonates that unconformably overlie the lower to

middle Paleozoic strata in the fault zone area of the Central Basin Platform is a good indication of the fault zone being active during this time (EIA, 2018). As a result of the uplift of the Central Basin Platform, there is varying subsidence and basin geometry in the Midland and Delaware Basins (EIA, 2018). The tectonic activity in the Central Basin Platform continued until the end of the Wolfcampian time and the basin subsidence continued until the end of the Permian time (EIA, 2018).

The Delaware Basin was structurally and topographically low during most of the Permian time (Sutton, 2014). This provided an inlet for marine water in the Delaware Basin (Sutton, 2014). By the Middle Permian, the Delaware Basin received minor sedimentation from the low coastal plains and became a host to reefs that were built by sponges, algae, and microbial organisms (Sutton, 2014). Deep water inputs and the organisms within the reefs formed a higher elevation area through carbonate buildups that allow a separation from the shallow water and deep-water deposits (Sutton, 2014). The Delaware Basin is about 2,000 feet deeper than the Midland Basin (Sutton, 2014). This difference in depth caused the sediments in the Delaware Basin to experience a pressure increase during burial (Sutton, 2014). Figure 2.2 is a depth map of the Delaware Basin, Central Basin Platform, and Midland Basin. This figure shows the Delaware Basin is deeper than other components of the Permian Basin. The depth factor is one of the leading causes of the stratigraphic differences between the Midland Basin and the Delaware Basin (Sutton, 2014)

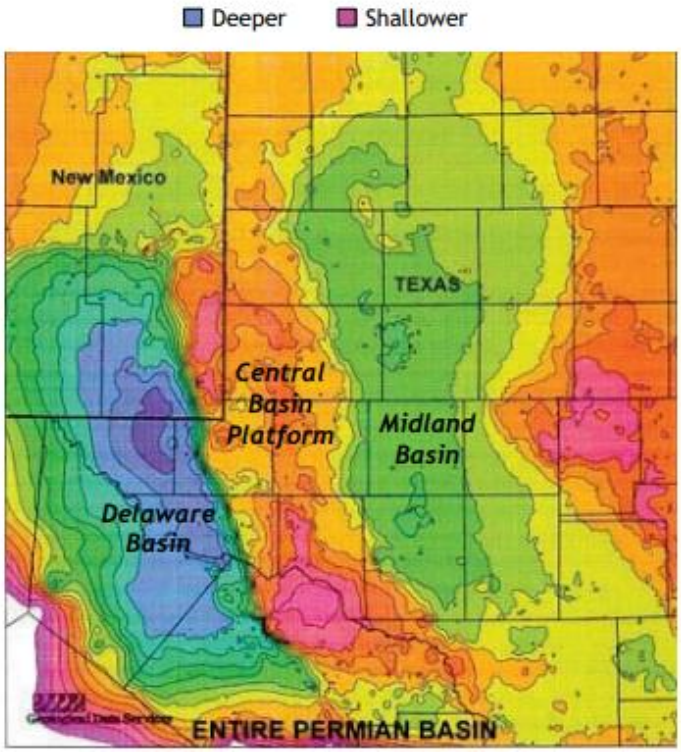

Figure 2.2: Depth map of the Delaware Basin, Central Basin Platform, and Midland Basin (from Fairhurst et Al., 2012).

2.1 Stratigraphy

The Permian Basin contains many formations within the three main sub-divisions. The stratigraphic description of the Bone Spring and Wolfcamp Formations within the Delaware Basin will be the focus of this study. Permian Basin rocks typically grade upwards from clastic-carbonate rocks into an evaporate sequence (EIA, 2018). These rocks are very heterogeneous. In the Delaware Basin, the upper half of the Permian strata is the Guadalupian and the Leonardian. This upper half of the basin is dissected by a series of stacked reef complexes (Menchaca, 2013). The lower half of the basin is made up of Bone Spring and Wolfcamp formations (Figure 2.3). The Wolfcamp Formation lies beneath the Bone Spring Formation. The contact between these

two formations are gradational, making it difficult to pick the top of the Wolfcamp Formation (Sloss, 1988),

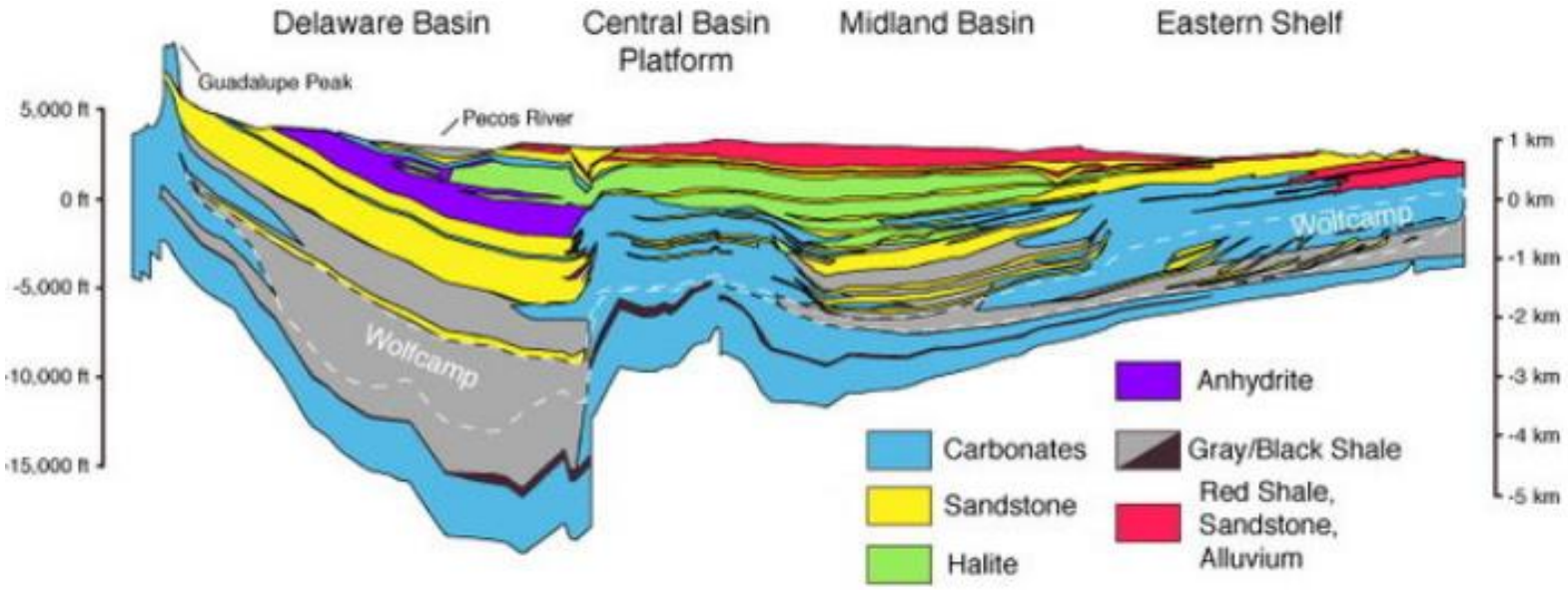

Figure 2.3: Generalized geologic cross section of the Permian Basin (Engle et. al, 2016).

The Bone Spring Formation is a hybrid shale-oil system that contains organic rich source rocks placed next to organic-lean reservoir layers like sandstone and carbonates (Jarvie, 2012). Both the reservoir and source rocks are thinly bedded. The Bone Spring Formation is roughly 3,500 feet thick (Menchaca, 2013). The Bone Spring Formation consists of three members: First Bone Spring, Second Bone Spring, and Third Bone Spring (Figure 2.4). All three members consist of a layer of predominately siliciclastic sediment alternating with a sequence of predominately carbonate allochthonous sediment (Gawloski, 1987). These alternating sequences are interbedded with siliciclastic, carbonate, and shale facies. The organic-rich layers of shale or carbonate are interlaminated with organic-rich sandstone or carbonate layers (Dutton et al., 2004). The sand layers are made up of fine to very fine, angular to sub-angular quartz (Dutton et

al., 2004). The carbonate members are mostly made up of mudstones and wackestones that became carbonate breccias due to debris flow (Dutton et al., 2004). The alternating sedimentation displayed in the Bone Spring Formation is a result of sea level changes, where marine transgression deposited carbonates and marine regression deposited clastics (Menchaca, 2013).

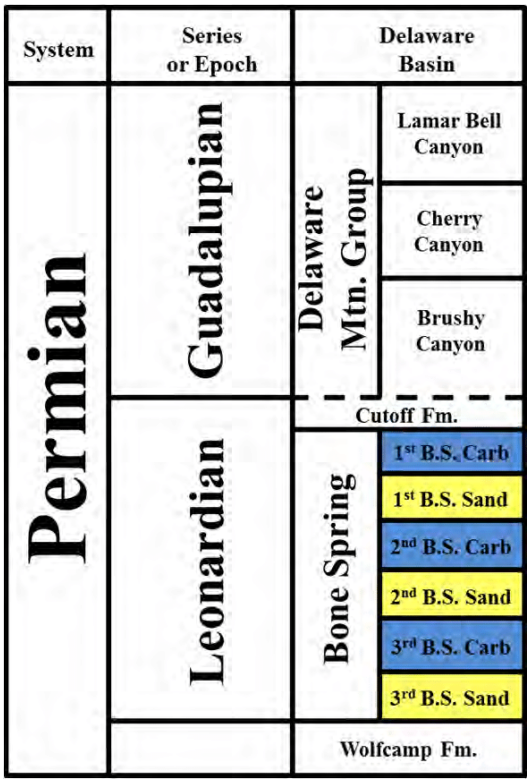

Figure 2.4: Stratigraphy of the Delaware Basin (from Grammer, 2013).

The Wolfcamp Formation in the Delaware Basin is very heterogeneous. The Wolfcamp Formation is also known as the basinal Wolfcamp, the strata are generally dark in color and contains carbonates that are typically lime packstones, wackestones and mudstones (Tyrrell, 1966). This formation is divided into three different units: (1) a lower detrital unit that fluctuates

in thickness and lithology; (2) a sequence of lime-shale-lime that is somewhat uniform in thickness and lithology; and (3) the Third Bone Spring with uniform thickness and lithology (Tyrrell, 1966). The basinal Wolfcamp represents a shift from a time of active tectonism to one of relative stability (Tyrrell, 1966).

Chapter 3

Methods

3.1 Acquisition and Preparation of Samples

The samples collected for this study were provided by the New Mexico Bureau of Geology & Mineral Resources (NMBGR) in Socorro, New Mexico. There is a total of ten samples that originate from three wells located in Lea County, New Mexico: Red Hills Unit Well No.1, Peoples Security Co. Well No.3, and State No.1. The ten samples are referred to by their sample ID (well short name and depth) during this study for consistency and simplicity (Table 1).

Table 1**:** Well names, formations and sample IDs used in this study (WF: Wolfcamp; BS: Bone Spring) (Text colors correspond to lithofacies from Figure 4.2).

Well Name	Formation	Sample ID	Sample Depth (Feet)
Red Hills Unit Well No. 1	Wolfcamp	RHU-13475-WC	13475
	Wolfcamp	RHU-13499-WC	13499
Peoples Security Co. Well No. 3	Wolfcamp	PSC-10499D-WC	10499
	Wolfcamp	PSC-10520A-WC	10520
	Wolfcamp	PSC-10588A-WC	10588
	Wolfcamp	PSC-10621A-WC	10621
State No. 1	First Bone Spring	ST-9201B-BS1	9201
	First Bone Spring	ST-9220C-BS1	9220
	Second Bone Spring	ST-10319B-BS2	10319
	Wolfcamp	ST-10732E-WC	10732

For this study, whole rock and microscopic photos were taken for all samples (Figure 3.1). Next, the samples were prepared in a variety of different sizes: cubes, half cubes, thin slabs (polished) and different size fractions (GRI + down to powder of <75 μm; GRI: Gas Research Institute). The powdered samples underwent XRD, pyrolysis and TOC analyses. Imbibition and mercury injection capillary pressure used 1-cm-sided cube sized samples. All tests performed in this study provides data that shows the pore size distribution, pore connectivity, and fluid interaction of the sample.

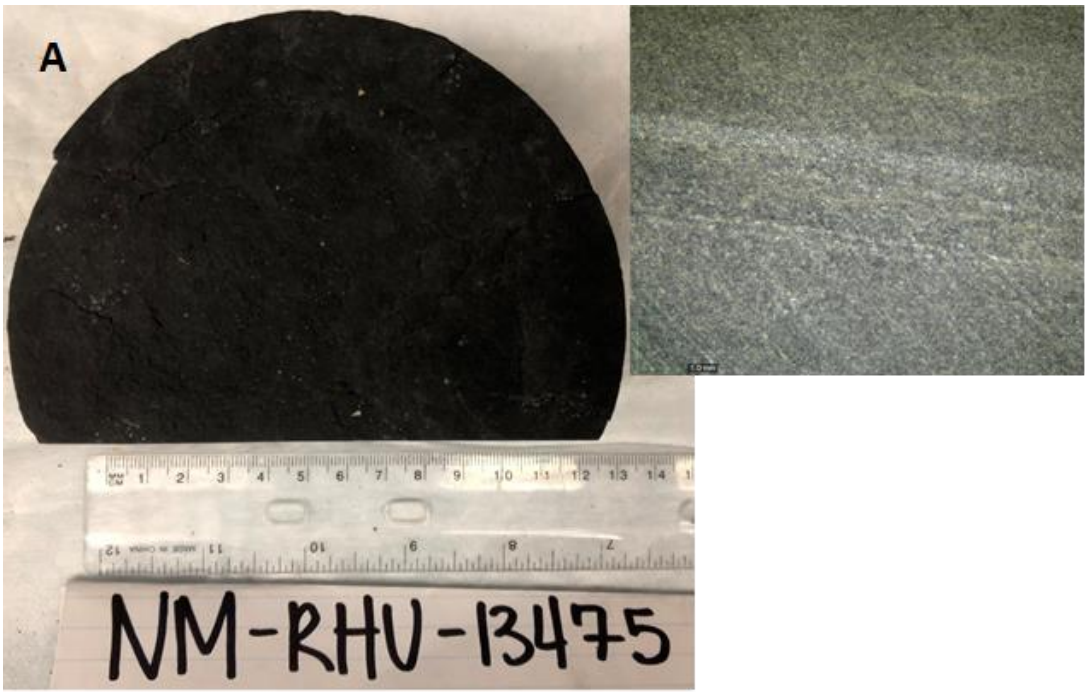
A
NM-RHU-13475

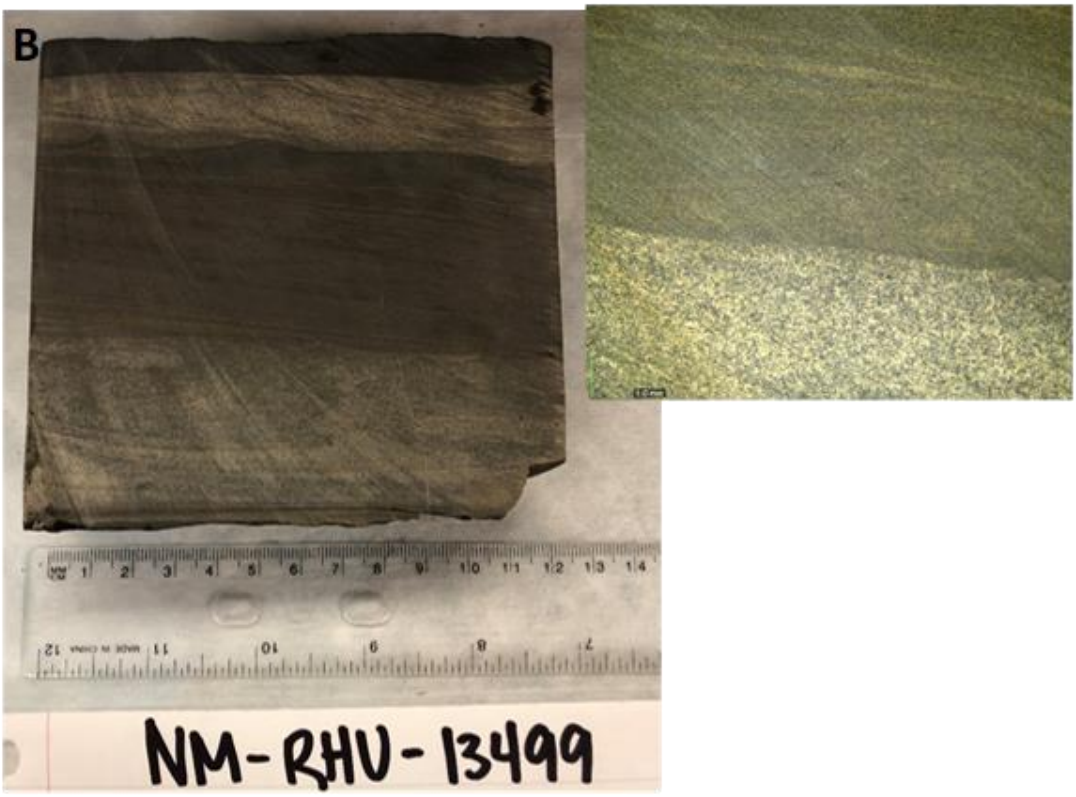
B
NM-RHU-13499


C
NM-PSC-10499D


D
NM-PSC-10520A

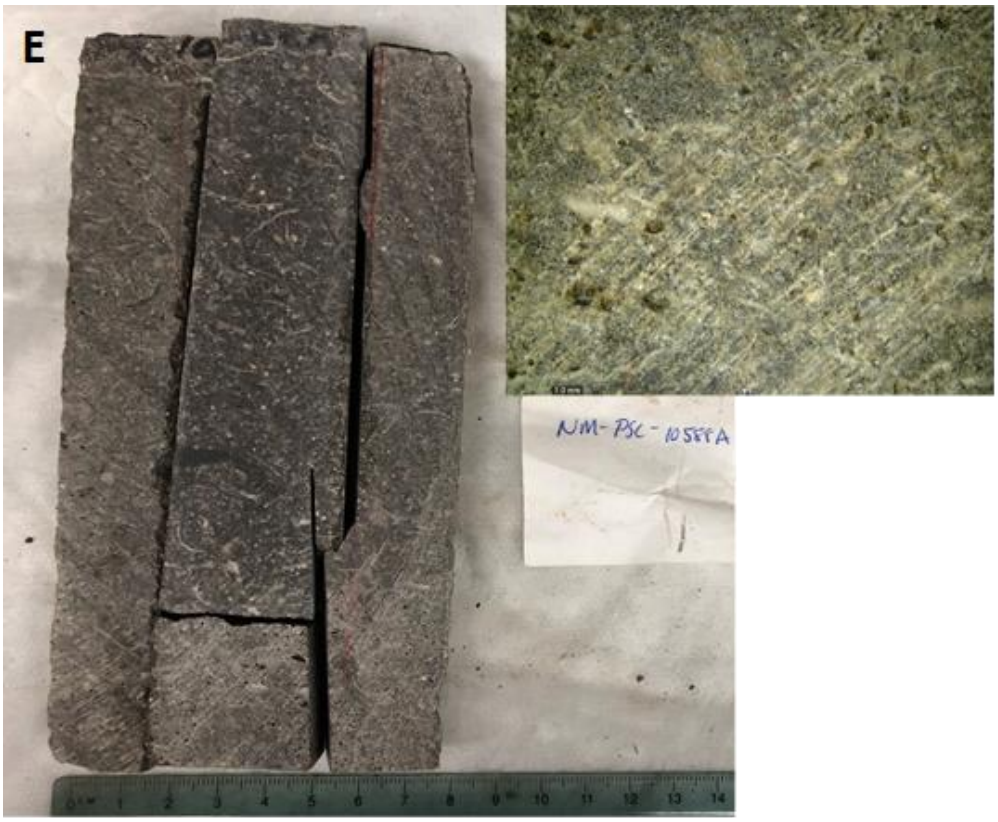
E
NM-PSC-10588A

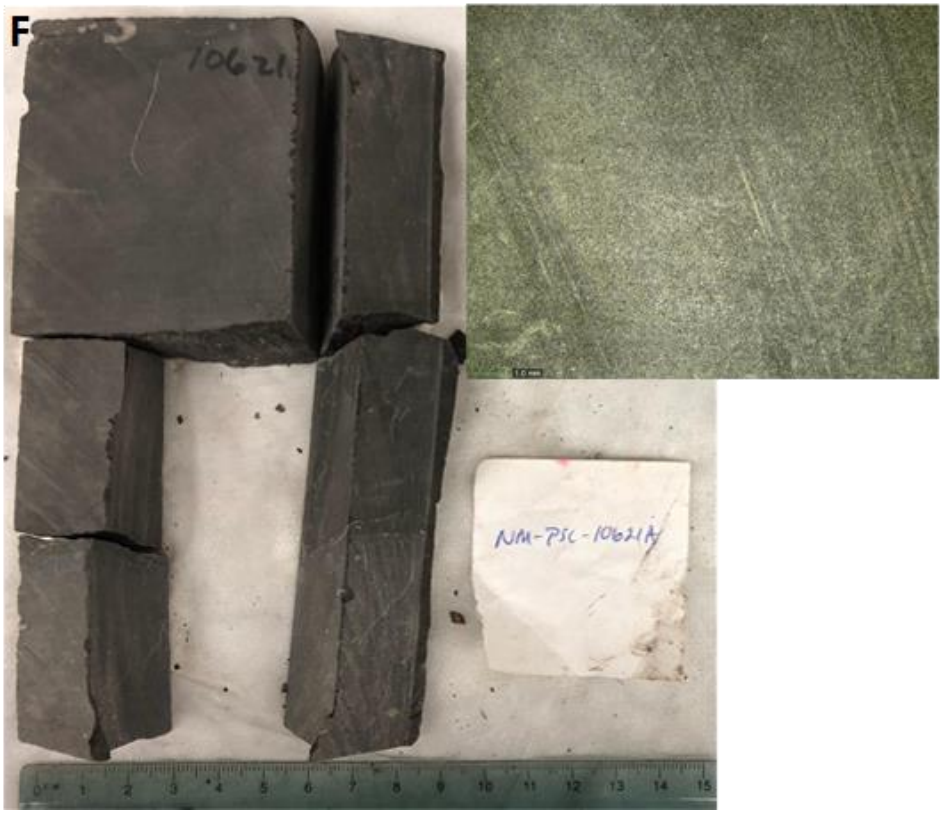
F
10621
NM-PSC-10621A


G
9201B
NM-ST-9201B

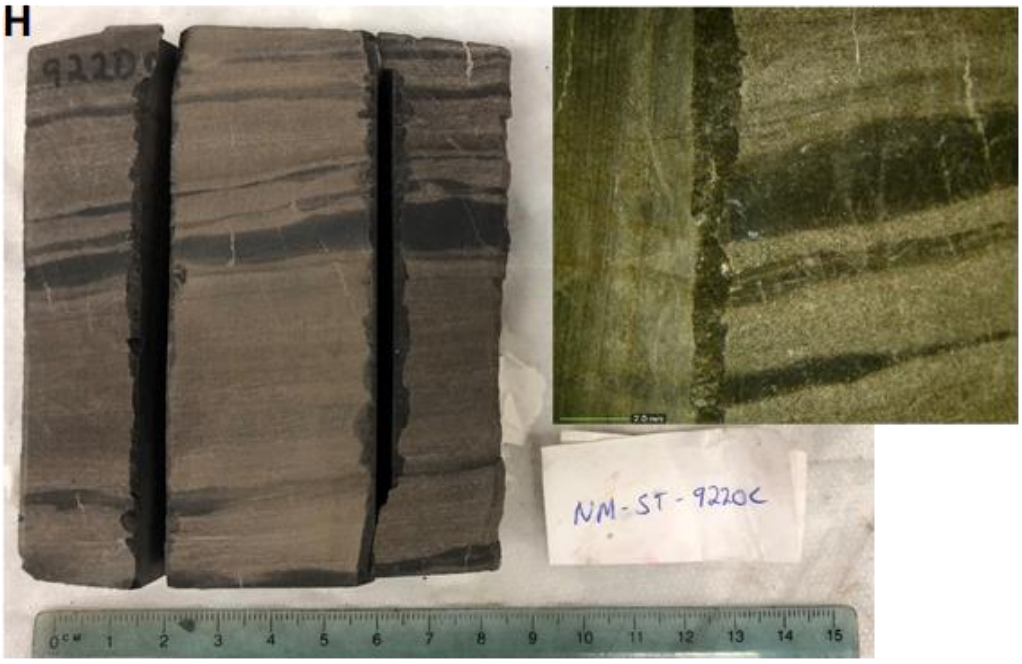
H
NM-ST-9220C


I
NM-ST-10319B


J
NM-ST-10732E

Figure 3.1: (A-J) Images of the whole rock and a part of the sample; NM: New Mexico.

3.2 XRD, TOC, and Pyrolysis

X-ray Diffraction (XRD) analysis was performed using the Shimadzu MAXima XRD-7000. The methods and procedures for XRD are attached in Appendix A. XRD results were used to relate the minerology of the sample to its pore structure. This analysis identifies the minerals and the weight percentages that are present in each sample. The XRD data were also used to estimate the lithology of the samples using the sCore Lithofacies ternary diagram.

Total organic carbon (TOC) and pyrolysis analysis were performed on all samples by GeoMark Research in Humble, Texas. The TOC analysis was performed using the LECO C230 instrument, while the HAWK instrument was used for pyrolysis analysis. The methods and procedures for TOC and pyrolysis are attached in Appendix B. Pyrolysis analysis provides S1, S2, S3 and T_{max} data. S1 represents the residual hydrocarbons left in the rock. S2 represents the remaining generation potential of hydrocarbons in the rock. S3 represents the organic carbon dioxide yield. T_{max} measures the thermal maturity after being converted into an equivalent vitrinite reflectance (Jarvie, 2012).

3.3 Vacuum Saturation and Liquid Displacement

Vacuum Saturation is an effective method utilized to study the pore structure and properties of a porous media. This method can quantify the edge-only accessible porosity of porous materials (Hu et al., 2015). The vacuum saturation apparatus quantifies the effective porosity by evacuating the sample chamber, and then immersing the sample in a fluid to occupy the evacuated pore space. Evacuating the sample chamber will provide access to the pores

connected to the edge of the sample (Kibria et al., 2017). Evacuation of the edge accessible pores of low-permeable samples occurs by producing a vacuum to 0.05 Torr, which is equivalent to 99.993% vacuum (Kibria et al., 2017). During fluid immersion, the sample was introduced to pressurized CO_2, further assisting the fluid into the pores of the sample. CO_2 is easier to dissolve in DI water than air, allowing for better saturation and porosity measurements. After vacuum saturation, the saturated samples underwent liquid displacement using the Archimedes Principle to determine the particle density for rock cores, large and irregularly-shaped rocks, and gravel (Dane et al, 2002). The data collected from vacuum saturation and liquid displacement are utilized in Eq. 1-5 to find bulk density, particle density, porosity, gravimetric water content, and volumetric water content (Dane et al., 2002).

$$p_b = W_d/V_b \quad \text{Eq. 1}$$

$$\phi = (W_s - W_d)/V_b \quad \text{Eq. 2}$$

$$p_p = W_d/(V_b - \phi) \quad \text{Eq. 3}$$

$$\theta_w = (W_i - W_d)/W_d \quad \text{Eq. 4}$$

$$\theta_v = \theta_w p_b \quad \text{Eq. 5}$$

Where,

p_b: bulk density of the sample (g/cm^3);

W_d: dry weight of the sample (g);

V_b: bulk volume of the sample (can be determined using Archimedes Principle) (cm^3);

ϕ: porosity of the sample (%);

W_s: saturated weight of the sample (g);

W_i: initial weight of the sample (g);

p_p: particle density of the sample (g/cm^3);

θ_w: gravimetric water content;

θ_v: volumetric water content.

Procedure for Vacuum Saturation

The apparatus used for vacuum saturation consists of a sample chamber connected to a compressed CO_2 gas cylinder and a vacuum pump. Prior to vacuum saturation, the shale sample was placed inside the 60°C oven for at least 48 hours and then placed in the desiccator to cool down. Next, the weight of the sample was recorded. Sample types for vacuum saturation included irregular size, core plugs, and 1 cm cubes. The cooled sample were placed in the chamber of the apparatus with the chamber lid tightly attached. After closing the chamber, the three-way valve between the compressed gas, sample chamber and the vacuum were opened towards the vacuum line. Then, the vacuum pressure gauge and the vacuum pump were turned on to begin the experiment. The pressure in the chamber dropped below 0.2 Torr after < 1 hour. The evacuation of the chamber continued for at least 8 hours. After the initial 8 hours, the three-way valve was turned towards the pressurized CO_2 gas line and the vacuum pump was turned off. The valve on the regulator of the pressurized gas tank was used to slowly release CO_2 into the chamber until the gauge read 50 psi; then we turned the three-way valve to the middle position so that it does not point towards the vacuum or gas tank. After, we turned the three-way valve towards the vacuum pump again and resumed the evacuation of the chamber for another 8 hours. Then the fluid reservoir was filled with enough deaired DI water to fully submerge the samples in the chamber by opening the valve connecting the fluid reservoir to release fluid into

the chamber. Next, we released CO_2 into the chamber to further pressurize the fluid into the pore space of the sample for at least 8 hours.

Procedure for Liquid Displacement

After the completion of vacuum saturation, the saturated samples underwent liquid displacement tests. The saturated sample was weighed in air by gently blotting off excess fluid with a slightly moist Kimwipe before weighing. Then, the sample was re-submerged in the saturating fluid (DI water) and re-weighed using the same process. The saturated sample was weighed twice in the fluid using the Archimedes Principle. The apparatus used for the Archimedes Principle consists of a wire basket that is suspended over a beaker of water (Figure 3.2) (Dane et al., 2002). The beaker of water was placed on a top loading balance. The balance was zeroed with the empty basket submerged in the beaker of water. The wire basket should only touch the water within the beaker, not the beaker or balance. Next, the wire basket was raised from the water, without displacing any water inside the beaker. The saturated sample was placed inside the wire basket and submerged into the beaker of water. Once the sample was completely submerged, the weight displaced on the balance was recorded. The recorded value is used to calculate the bulk volume of the sample.

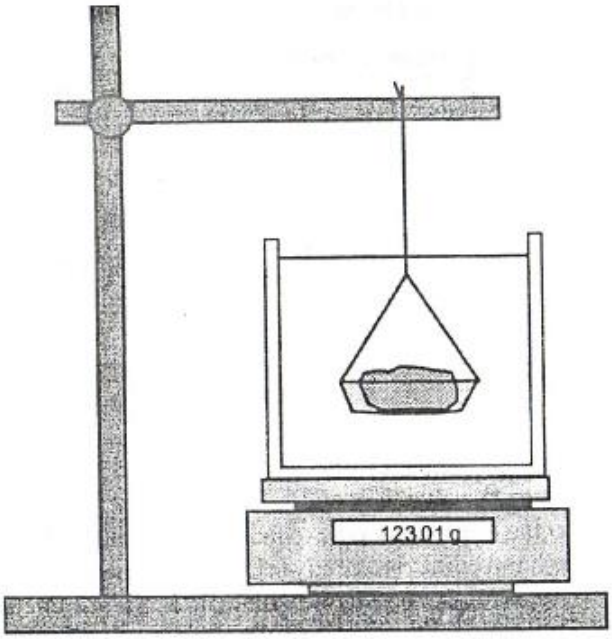

Figure 3.2: Apparatus used for volume displacement using Archimedes Principle (from Dane et al., 2002).

3.4 Mercury Injection Capillary Pressure (MICP)

MICP is a method that utilizes non-wetting mercury to invade the pore throats by overcoming the capillary pressure of up to 60,000 psia (413 MPa) through applied external pressures. The MICP analysis was performed with the apparatus Micromeritrics Autopore IV 9520 (Figure 3.3). The sample was submerged in liquid mercury that has a high surface energy (Hu et al., 2015). After submersing the sample, a pressure was applied, allowing the liquid mercury to invade the pores of the sample (Hu et al., 2015). Smaller pores require higher pressures for the liquid mercury to invade (Hu et al., 2015). This is a useful technique to analyze pore-throat sizes between 500 μm to 3.5 nm (Giesche, 2006). The porosimeter produces the highest pressure at 60,000 psia (413 Mpa) (Hu et al., 2015). The highest pressure corresponds to a pore-throat diameter of ~3 nm by the Washburn equation (Hu et al., 2015). The Washburn

equation (Eq. 6) determines the pressure to pore throat relationship. This determination is made with the assumption that all pores of the sample are cylindrical (Hu et al., 2015). The assumption that the pores are cylindrical are unrealistic but provides an applicable representation of the pore distribution for petrophysical studies (Quintero, 2016).

$$\Delta P = -\frac{2\gamma cos\theta}{r} \quad \text{Eq. 6}$$

Where,

ΔP- Difference in pressure (psia);

γ- Surface tension for mercury (dynes/cm);

θ- Contact angle between porous media and mercury (degrees);

r- Corresponding pore throat radius (μm).

The Washburn equation has since been modified by the works of Wang et al. (2016). The modification of the Washburn equation is due to the varying contact angle and surface tension values that the original equation did not consider (Mann, 2017). According to Wang's work, the varying contact angle and surface tension values begin when the pore throat diameter falls below 10 nm (Wang et. al, 2016). The modified Washburn equation presented in the Wang's (2016) work is shown in Eq. 7 (Wang et al., 2016).

$$\Delta P = -(\frac{2\gamma Hg(r) cos\theta Hg(r)}{r}) \quad \text{Eq. 7}$$

MICP data provides bulk density, particle density, porosity, pore throat diameter distribution, and total pore surface area of the samples (Hu et al., 2015). In addition, MICP data was used to indirectly obtain permeability and tortuosity (Hu et al, 2015). Permeability was estimated using the equation proposed by Katz and Thompson (Eq. 8) (Hu et al., 2015):

$$k = \frac{1}{89}(L_{max})^2 \left(\frac{L_{max}}{L_c}\right) \phi S(L_{max}) \quad \text{Eq. 8}$$

Where,

k- Absolute permeability (μm^2);

L_{max}- Pore throat diameter at the maximum hydraulic conductance (μm) (when capillary pressure is overcome at a specific pore diameter and mercury percolates through the sample)

L_c- Characteristic length (μm) of the pore throat diameter corresponding to the threshold pressure (determined from the inflection point of the cumulative intrusion curve);

ϕ- Porosity of the sample (%);

$S(L_{max})$- Mercury saturation at L_{max} (Gao and Hu, 2013).

Tortuosity was empirically determined using MICP data in Eq. 9 (Hu et al., 2015).

$$\tau = \sqrt{\frac{p}{24k(1+pV_{tot})} \int_{\eta=r_{c,}min}^{\eta=r_{c,}max} n^2 f_v(n) dn} \quad \text{Eq. 9}$$

Where,

τ – Effective tortuosity (dimensionless);

p – sample density ($g/(cm^3)$);

V_{tot} – Total pore volume (mL/g);

$\int_{\eta=r_{c,}min}^{\eta=r_{c,}max} n^2 f_v(n) dn$ – Pore throat volume probability density function.

Procedure for MICP Test

Prior to performing MICP, each sample was oven dried for at least 48 hours at 60°C. Oven drying samples removes the moisture in the pore spaces of the sample. Then, samples were placed in a desiccator to cool to room temperature. After cooling down, the sample was placed into a penetrometer, which is a sample chamber that is connected to a metal clad precision-bore, glass capillary system. Next, the penetrometer was placed and sealed in the low-pressure port and excavated to 6.7 Pa (99.9993% vacuum) to remove air and moisture (Hu et al., 2015).

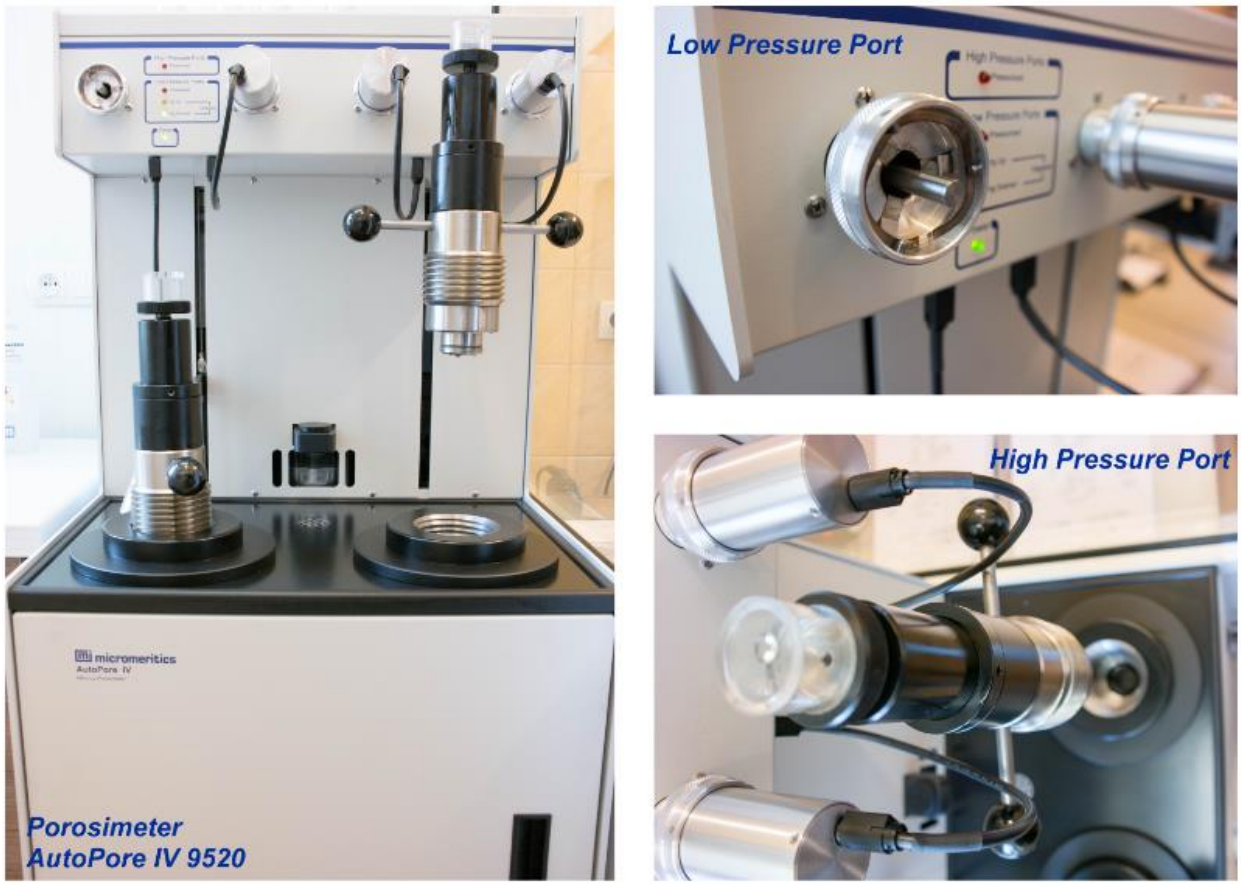

Figure 3.3: Micromeritrics Autopore IV 9520 (left); the low-pressure port on the (top right), and the high-pressure port (bottom right) on the apparatus.

After evacuation, the penetrometer was filled with liquid mercury at a reduced pressure (Giesche, 2006). As the pressure slowly increased, the mercury began to invade the largest pores. As mercury invades the pores, the mercury column in the stem shortens until low-pressure intrusion is complete. After low-pressure intrusion, the weight of the penetrometer, filled with the sample and liquid mercury, was determined (Giesche, 2006). The weight of the penetrometer was used to calculate the bulk density of the sample. Next, the penetrometer was transferred to the high-pressure port for the remainder of the experiment (Giesche, 2006). The pressure during high-pressure intrusion will increase up to 60,000 psia (413 MPa). During the pressure increase, the volume of mercury that intruded into the pores were monitored at a detection limit of <0.1 µL (Quintero, 2016). After completion of the experiment, pore-throat size distribution, permeability and tortuosity were determined using the MICP data.

3-5 Spontaneous Imbibition

Spontaneous imbibition is a method that allows the nonwetting fluid in a porous medium to be displaced by a wetting fluid through capillary forces (Gao and Hu, 2011). The wetting fluids were DI water and DT2 (n-decane: toluene= 2:1 in volume). The capillary pressure is dependent on the wettability of the sample, and the permeability is dependent on the porosity and pore connectivity of the sample. Therefore, the fluid, porous media, and the fluid-rock interactions are the properties that the rate of imbibition rely on. The cumulative uptake of fluid by imbibition can be expressed by Eq. 10 (Hu et al., 2001). The "At" in Eq. 10 can be ignored if the gravity is negligible compared to capillarity (Tokunaga and Wan, 2001).

$$I(t)=St^{0.5}+At \qquad \text{Eq. 10}$$

Where,

I(t): cumulative imbibition (m) as a function of time;

t: time (s);

S: sorptivity ($ms^{0.5}$);

A: empirically determined constant that relies on the medium properties, initial water content, and boundary conditions (m/s).

Guided with the percolation theory, results from spontaneous imbibition can help assess the sample's pore network connectivity. The percolation theory predicts that an infinite number of pores exist within a medium, but only a fraction of these pores are active or connected (Ewing et al., 2002). The pore connectivity is assessed using the slope of the log imbibed liquid mass vs. the log time (Hu et al., 2012). For this study, a slope range of ~0.25 or ~0.5 identifies a sample's pore connectivity. A slope of ~0.25 indicates that pore connectivity is barely above the percolation threshold for the fluid to move across the domain through the connected pores. A slope of ~0.50 indicates that the sample has well-connected pores. Although the percolation theory was mentioned to classify pore connectivity, details of this theory are outside the scope of this study.

Procedure for Spontaneous Imbibition

Prior to the imbibition test, the cubes must undergo sample preparations. The cubes were covered with quick-cure epoxy, leaving the top and bottom of the cubes bare. The quick-cure epoxy on the cube prevents fluid evaporation/uptake on the sides of the samples during imbibition. Then, the sample were dried at 60°C for at least 48 hours. The oven dried samples

went into a desiccator for a minimum of 10 minutes to cool down before starting the experiment. While the sample was in the desiccator, a petri dish was partially filled with the imbibing fluid. The partially filled petri dish was weighed with its mass and put inside the imbibition chamber. Additional beakers of DI water for the DI water runs were placed inside the chamber to keep the humidity of the chamber above 98%. Figure 3.4 shows the apparatus used to measure imbibition. The cooled cube was placed in a custom-made holder and placed inside the chamber. Inside the chamber, the holder was connected, by a hook, to a bottom-weighing electronic balance, which was connected to a computer that received weight measurements during the experiment. The chamber door was closed once imbibition was ready to start. An adjustable jack raised the closed chamber until the sample bottom was in contact with the fluid in the petri dish. Once the sample bottom touches the fluid, the balance began sending weight measurements to the computer to be recorded based on the set time interval. The time intervals used for imbibition were: every second for 2 minutes, then every 30 seconds until 1 hours, then 2 minutes until 6 hours, and 5 minutes until the end of the experiment. The DI water imbibition tests were performed for 24 hours and the DT2 tests for 8 hours.

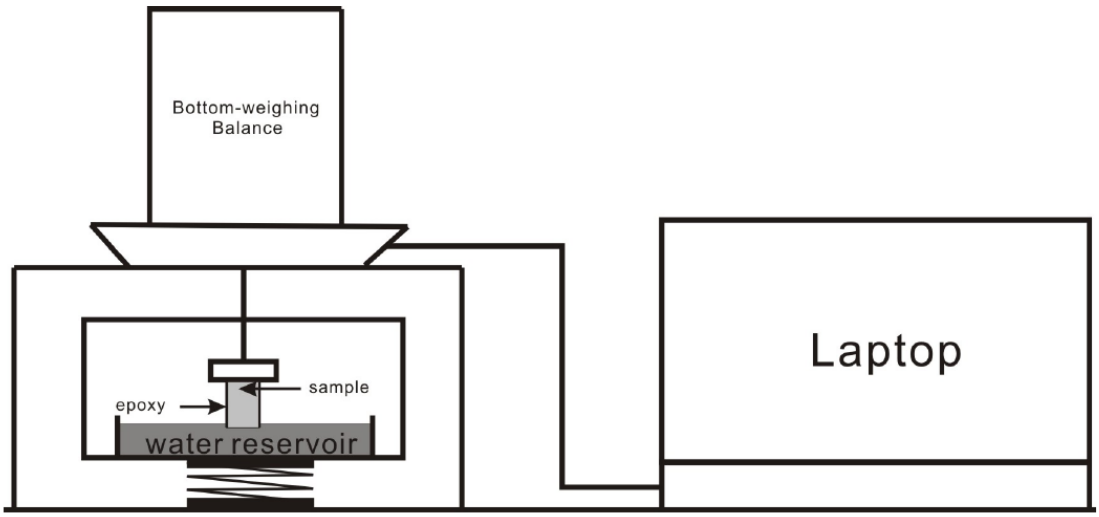

Figure 3.4: Apparatus used for imbibition (Gao and Hu, 2012).

After the imbibition run was complete, the adjustable jack was lowered to move the sample away from the fluid in the petri dish. The excess fluid on the sample was quickly wiped off with a damp Kimwipe and weighed. Then, the sample and the sample holder were weighed. The weighed measurements provide a check against the buoyancy effects and any condensed fluid on the sample holder. Lastly, the fluid and the petri dish were weighed, which shows the effects of evaporation and provides a check against the cumulative imbibition measured by the computer.

The data was plotted with the log cumulative imbibition vs. log time. The measurements that were taken before and after imbibition testing were used to consider any buoyancy and evaporation. The log-log plot has several slope lines that were used to best fit the different time periods.

3-6 Production Data

Annabelle Lopez from the New Mexico Bureau of Geology & Mineral Resources (NMBGR) was very helpful with providing the production data for the wells of interest. The production data, history and general information on the wells were gathered by the New Mexico Oil Conservation Division. In addition, Drilling Info's Pro database was used for production and other well information.

Chapter 4

Results

4.1 Mineralogy

X-ray diffraction was performed on all 10 samples. The major minerals that are heavily present in the samples are quartz and carbonate minerals. Most samples have a clay content less than 14.2%. PSC-10499D-WC (~24% clay) is the only sample that does not have a relatively low clay content. Other trace minerals that are present are albite, microcline, ankerite, pyrite, anhydrite, ulvospinel, and illite (Figure 4.1). Table 2 shows the breakdown of the mineral weights (%) of each sample. The lithologies of the samples were determined using the sCore lithofacies classification scheme for organic mudstones and the mineral weights (%) from the XRD data (Figure 4.2). The samples that are within the Wolfcamp formation have several different lithofacies. The four lithofacies are carbonate dominated lithotype, carbonate-rich siliceous mudstone, mixed siliceous mudstone, and silica-rich carbonate mudstone. The samples in the First Bone Spring are clay-rich siliceous mudstone and silica-rich carbonate mudstones. Lastly, the Second Bone Spring is a carbonate dominated lithotype.

Table 2: Summary of the mineral content (%) and corresponding sCore Lithofacies (Colors represent and correspond to the lithofacies on Figure 4.2)

Sample ID	Quartz	Albite	Microcline	Calcite	Dolomite	Ankerite	Pyrite	Anhydrite	Ulvospinel	Illite	Lithofacies
ST-9201B-BS1	59.5	7.3	6.9		8.9		2.5	0.8		14.2	Clay-rich siliceous mudstone
ST-9220C-BS1	30.7	2.2		1	60.3		1.4			4.4	Silica-rich carbonate mudstone
ST-10319B-BS2	1.2				97			1.8			Carbonate dominated lithotype
ST-10732E-WC	4.1			80.2	15.7						Carbonate dominated lithotype
PSC-10499D-WC	44.6	4.2	3.7	1.6	20.6			1.3		24	Mixed Siliceous mudstone
PSC-10520A-WC	11.5	1.9			81.6	2.5	1			1.5	Carbonate dominated lithotype
PSC-10588A-WC	3				96.4			0.6			Carbonate dominated lithotype
PSC-10621A-WC	41.9	3.8		1	37.8		3.1		3	9.5	Carbonate-rich siliceous mudstone
RHU-13475-WC	33.7	5.1		7.8	43.5	7		0.7		2.2	Silica-rich carbonate mudstone
RHU-13499-WC	47.9	3		36.5	7.1		1.2			3.5	Carbonate-rich siliceous mudstone

A.

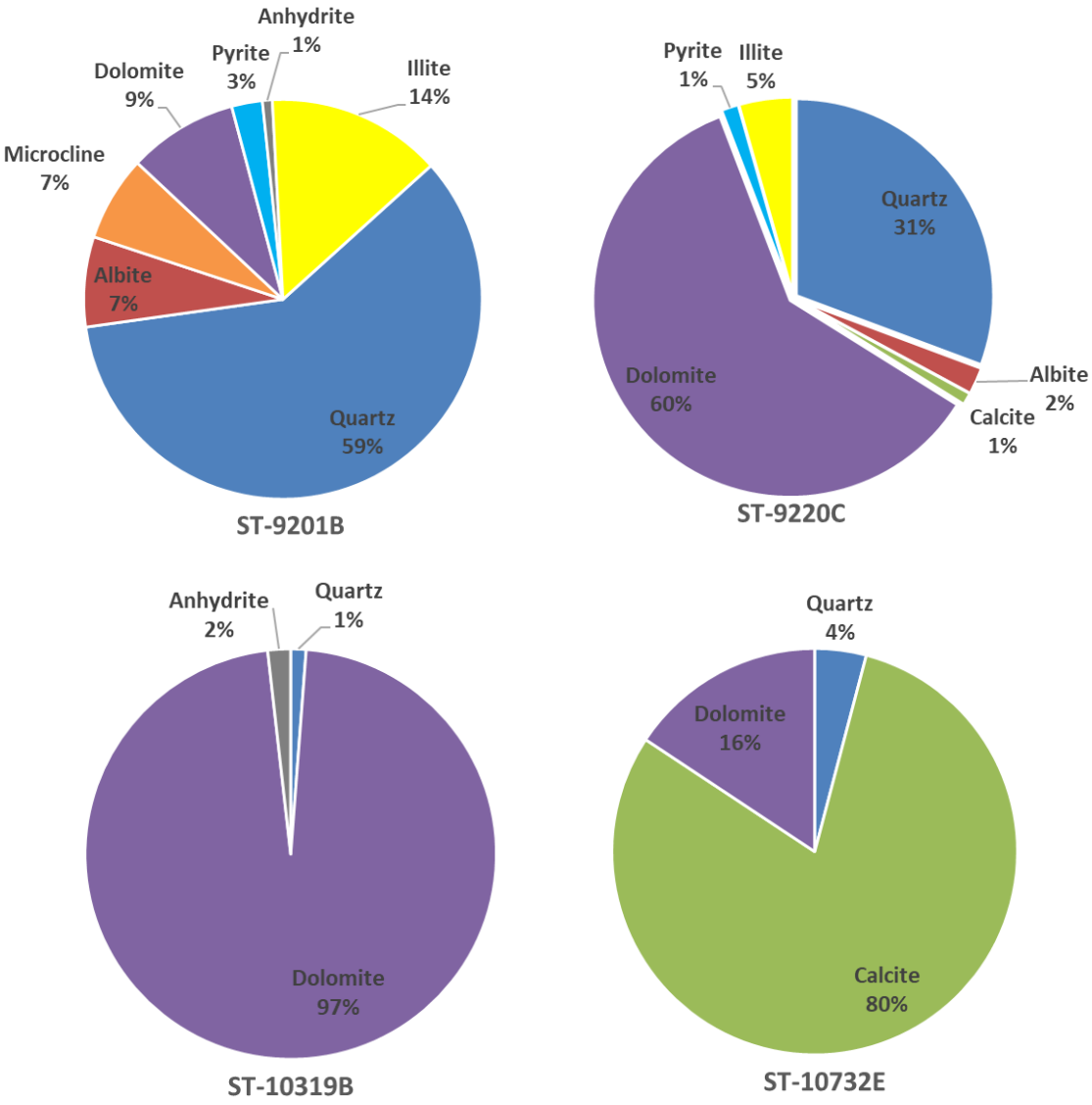
Anhydrite 1%
Pyrite 3%
Illite 14%
Dolomite 9%
Microcline 7%
Albite 7%
Quartz 59%
ST-9201B
Pyrite 1%
Illite 5%
Quartz 31%
Albite 2%
Dolomite 60%
Calcite 1%
ST-9220C
Anhydrite 2%
Quartz 1%
Dolomite 97%
ST-10319B
Quartz 4%
Dolomite 16%
Calcite 80%
ST-10732E

B.

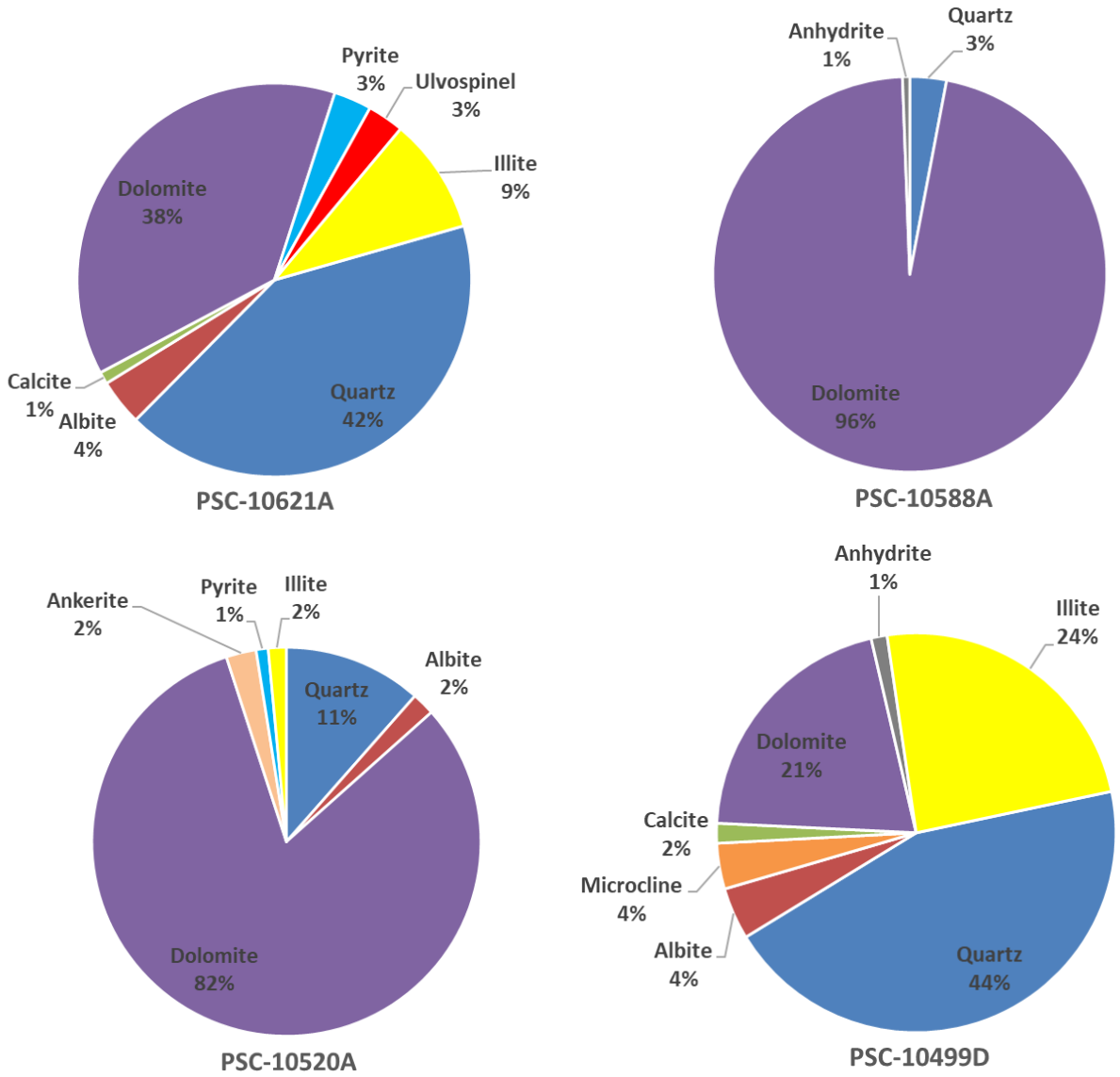
Pyrite 3%
Ulvospinel 3%
Illite 9%
Dolomite 38%
Calcite 1%
Albite 4%
Quartz 42%
PSC-10621A
Anhydrite 1%
Quartz 3%
Dolomite 96%
PSC-10588A
Ankerite 2%
Pyrite 1%
Illite 2%
Albite 2%
Quartz 11%
Dolomite 82%
PSC-10520A
Anhydrite 1%
Illite 24%
Dolomite 21%
Calcite 2%
Microcline 4%
Albite 4%
Quartz 44%
PSC-10499D

C.

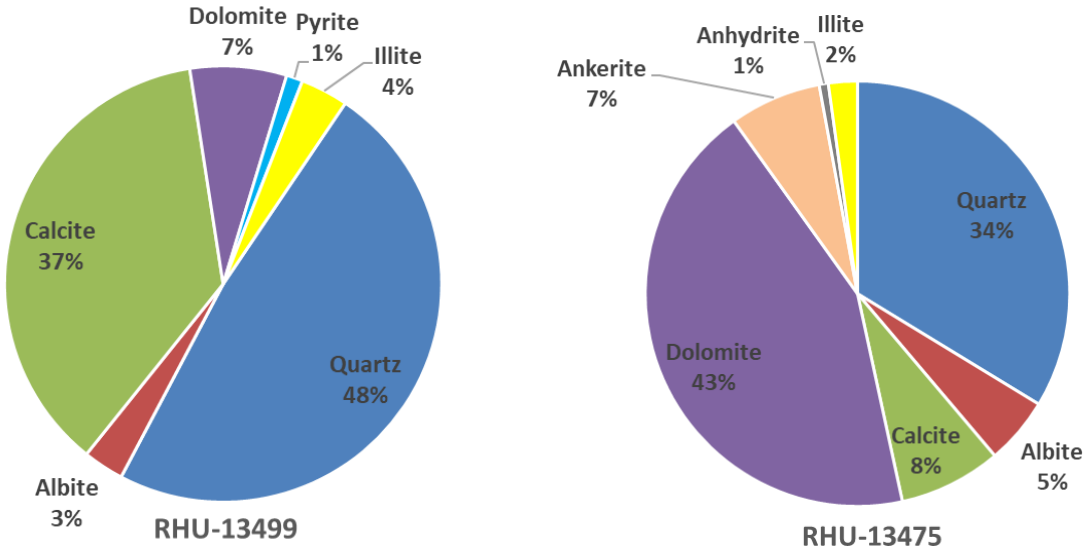

Figure 4.1: XRD results for samples in wells State No. 1 (A), Peoples Security Co. Well No. 3 (B), and Red Hills Unit Well No.1 (C).

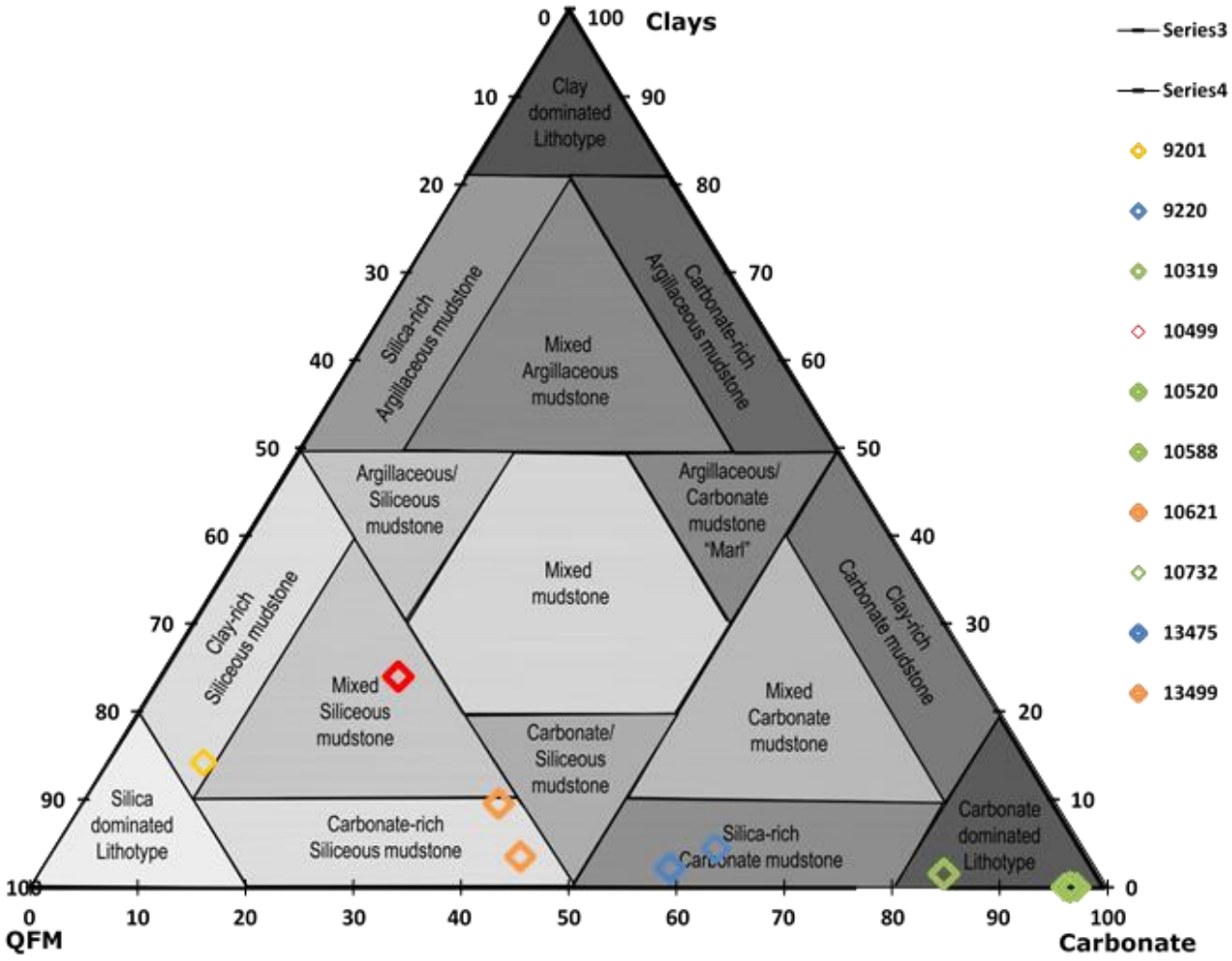

Figure 4.2: sCore lithofacies classification scheme diagram for 10 samples from three wells (modified from Gamero-Diaz, 2013).

4.2 Geochemistry

Pyrolysis and TOC analyses were performed on all 10 samples from three wells. Geochemical data for all samples are listed in Table 3. The TOC for all samples range from 0.08% to 1.96%. The residual hydrocarbons left in the rock (S1) range from 0.04 to 0.69 mg HC/g. The hydrogen index (HI) and the oxygen index (OI) values were used to identify the kerogen types. Type II and III kerogens are present in the samples (Figure 4.3). Type II kerogen is composed of marine algae and more prone to produce oil/gas. Type III kerogen is composed of vitrinite and more prone to produce gas (Curtis et al., 2013).

Table 3: Pyrolysis results for all samples.

Sample ID	TOC (wt.%)	S1 (mg HC/g)	S2 (mg HC/g)	S3(mg CO_2/g)	Tmax (°C)	Vitrinite Equivalency (from T_{max})	HI (mg HC/g TOC)	OI (mg CO_2/g TOC)
RHU-13475-WC	0.84	0.24	0.75	0.31	419	0.38	89	37
RHU-13499-WC	0.41	0.28	0.65	0.26	415	0.31	159	63
PSC-10499D-WC	1.02	0.69	1.49	0.31	446	0.87	146	30
PSC-10520A-WC	0.87	0.22	1.67	0.29	445	0.85	192	33
PSC-10588A-WC	0.10	0.04	0.08	0.21	439	0.74	80	210
PSC-10621A-WC	1.68	0.46	2.57	0.24	452	0.98	153	14
ST-9201B-BS1	0.26	0.12	0.34	0.18	424	0.47	131	69
ST-9220C-BS1	1.96	0.57	5.45	0.25	444	0.83	278	13
ST-10319B-BS2	0.08	0.05	0.08	0.22	436	0.69	100	275
ST-10732E-WC	0.21	0.10	0.22	0.26	448	0.90	105	124

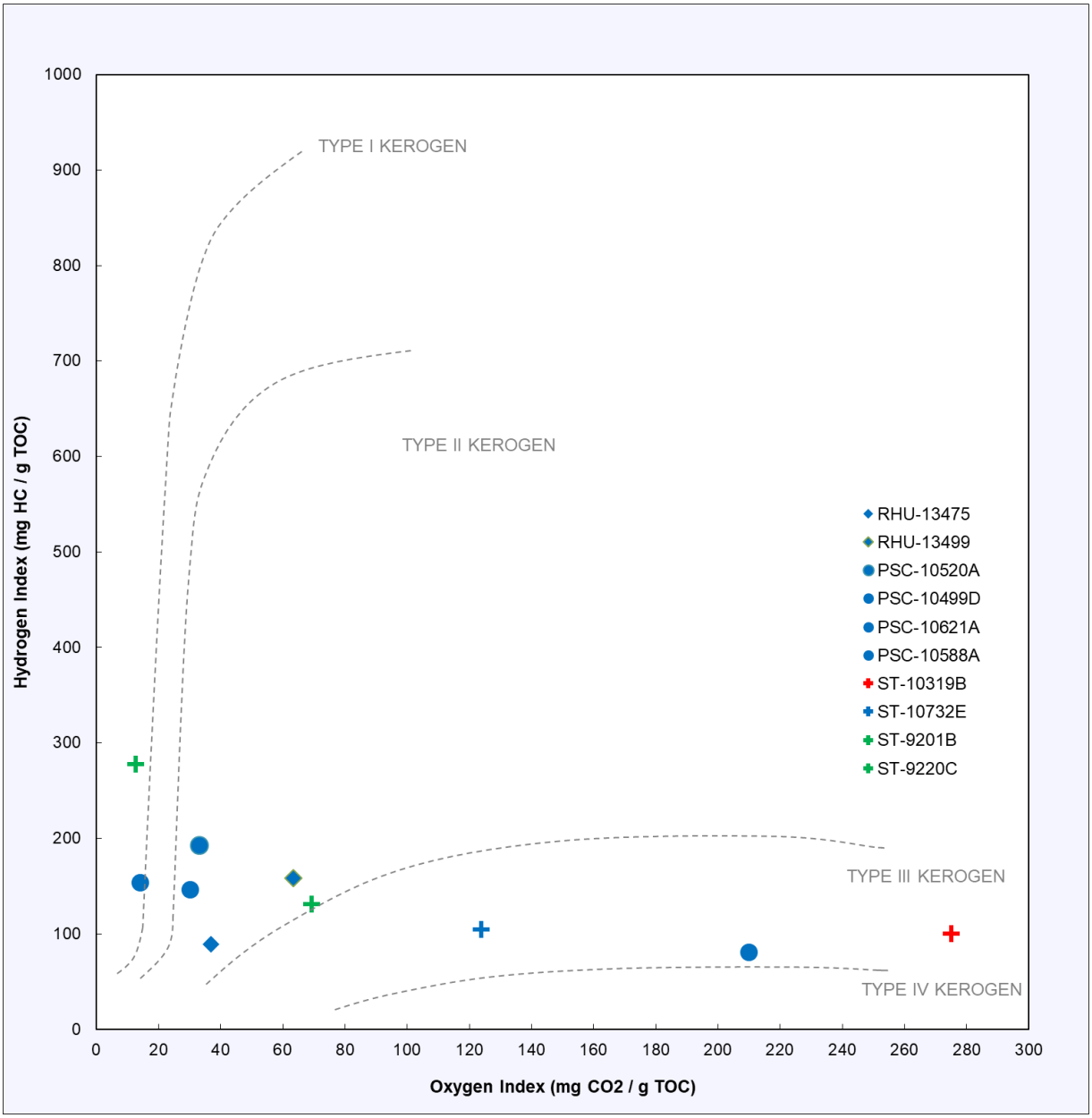

Figure 4.3: Kerogen types for all ten samples in this study.

4.3 Vacuum Saturation

Vacuum saturation measurements are used to determine the bulk density, grain density and the porosity of the sample. Table 4 shows the compiled results from vacuum saturation of irregularly sized samples and 1-cm cube sized samples using DI water as the saturating fluid. For most of the samples, the porosity appears to increase as the size of the sample decreases. The two samples where the porosity did not increase with a smaller sample size were PSC-10621A-WC and PSC-10520A-WC. The increase in porosity can be related to the pores becoming more accessible as the sample size becomes smaller.

Table 4: Vacuum saturation results for irregularly-sized and 1-cm cube samples.

	Irregularly sized (equivalent spherical diameter 5-9 cm)			**1-cm cube**		
Local sample ID	Bulk density (g/cm^3)	Grain density (g/cm^3)	Porosity (%)	Bulk density (g/cm^3)	Grain density (g/cm^3)	Porosity (%)
RHU-13475-WC	2.564	2.603	1.499	2.520	2.664	5.381
RHU-13499-WC	2.575	2.606	1.191	2.582	2.619	1.421
PSC-10499D-WC	2.515	2.554	1.518	3.087	3.180	2.830
PSC-10520A-WC	2.552	2.569	0.665	2.723	2.740	0.608
PSC-10588A-WC	2.251	2.285	1.487	2.701	2.793	3.299
PSC-10621A-WC	2.194	2.213	0.860	2.589	2.609	0.768
ST-9201B-BS1	2.101	2.234	5.953	2.415	2.578	6.334
ST-9220C-BS1	2.617	2.632	0.545	2.602	2.623	0.800
ST-10319B-BS2	2.213	2.317	4.515	2.630	2.783	5.487
ST-10732E-WC	2.205	2.219	0.606	2.628	2.650	0.827

4.4 Mercury Intrusion Capillary Pressure

MICP measurements can directly determine the pore-throat size distribution in the sample. Secondary parameters such as permeability and tortuosity were indirectly calculated by implementing the methods detailed by Gao and Hu (2013). Table 5 shows main pore structure characteristics obtained through MICP. MICP inflection points and the Washburn equation were used to determine the pore-throat size distribution for the connected pore-networks. An inflection point, shown as a peak in a plot of log differential intrusion vs. intrusion pressure, represents the point in which the mercury intrusion enters into a specific pore throat system. The method behind selecting the inflection point was outlined by Gao and Hu (2013). Figure 4.4 indicates an inflection point with colored arrows.

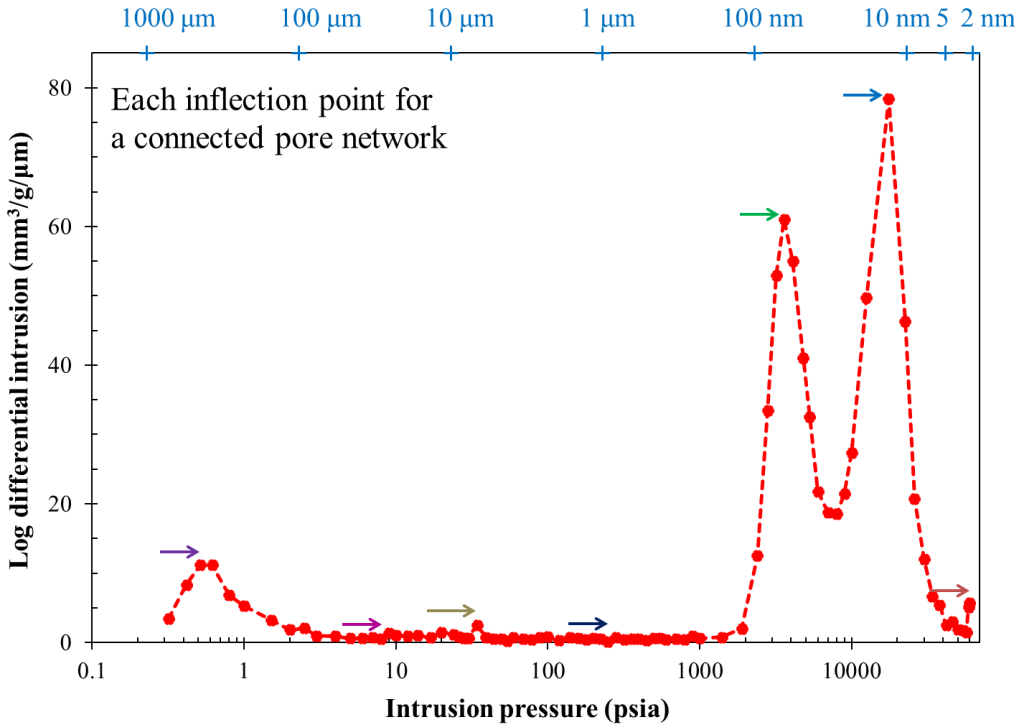

Figure 4.4: MICP intrusion results with multiple inflection points indicated by colored arrows.

Table 5: MICP-derived pore structure characteristics of all ten samples.

Sample ID	Sample Size	Bulk density (g/cm^3)	Skeletal density (g/cm^3)	Porosity (%)	Total pore area (m^2/g)	Total pore volume (mm^3/g)
RHU-13475-WC	1-cm cube	2.48	2.64	5.83	4.66	23.50
RHU-13499-WC	1-cm cube	2.53	2.60	2.36	5.02	9.30
PSC-10499D-WC	1-cm cube	2.72	2.76	1.38	0.15	5.08
PSC-10520A-WC	1-cm cube	2.79	2.80	0.36	0.29	1.30
PSC-10588A-WC	1-cm cube	2.70	2.87	5.90	6.10	21.80
PSC-10621A-WC	1-cm cube	2.63	2.64	0.49	0.42	1.90
ST-9201B-BS1	1-cm cube	2.45	2.62	6.44	2.69	26.30
ST-9220C-BS1	1-cm cube	2.52	2.66	5.23	7.92	20.70
ST-10319B-BS2	1-cm cube	2.62	2.84	7.65	4.95	29.20
ST-10732E-WC	1-cm cube	2.68	2.69	0.55	0.21	2.00

All samples have gone through one run of MICP analysis. Samples ST-10732E-WC, PSC-10621A-WC, and PSC-10520A-WC have low porosities that range from 0.36%-0.55%; all three samples are in the Wolfcamp formation. Samples RHU-13475-WC, RHU-13499-WC, PSC-10588A-WC, ST-9201B-BS1, ST-9220C-BS1, PSC-10499D-WC, and ST-10319B-BS2 have porosities that range from 1.38%-7.65%. These samples are in the First Bone Spring, Second Bone Spring, and Wolfcamp formation.

The pore throat diameters are quantitatively associated with different pore types. The related pore types and pore throat diameters are: (1) Pore throat diameters between 1000-1 micrometers are micro-fractures within the rock; (2) 0.5-1 micrometer are intergranular pore space; (3) 50-10 nanometers are intragranular pore space; (4) 10-5 nanometer sized pores are organic pores; (5) 5-2.8 nanometer are inter-clay platelet pore spaces. Table 6 and Figure 4.5 show the pore throat diameter (%) from MICP analyses. For RHU-13499-WC, RHU 13475-WC

and ST-10732E-WC, most of the pores are occupied by intragranular pores. A majority of PSC-10588A-WC and ST-9201B-BS1 pores are occupied by intergranular pores. The rest of the samples have pores that are mostly occupied by microfractures within the rock. In this study, the pore-throat network intervals 2.8-50 nm and >100 nm were examined.

Table 6: Pore-throat diameter (%) from MICP analyses for all samples.

	>10 µm	1-10 µm	0.1-1 µm	50-100 nm	10-50 nm	5-10 nm	2.8-5 nm
RHU-13475-WC	35.84	2.85	2.10	0.94	50.42	6.76	1.09
RHU-13499-WC	1.65	2.85	3.50	1.92	39.56	37.54	12.70
PSC-10499D-WC	32.63	32.63	16.33	3.38	11.93	10.98	17.48
PSC-10520A-WC	21.14	27.66	6.03	0.08	8.50	25.14	11.44
PSC-10588A-WC	22.89	13.46	24.44	2.11	10.22	14.44	12.45
PSC-10621A-WC	23.97	25.82	14.26	6.08	10.54	7.92	11.42
ST-9201B-BS1	13.63	0.80	44.76	13.35	23.15	4.31	0.02
ST-9220C-BS1	45.05	3.27	1.21	0.53	12.27	19.86	17.81
ST-10319B-BS2	31.18	26.24	18.19	1.26	6.66	9.40	7.08
ST-10732E-WC	12.31	16.76	17.40	14.58	19.53	17.71	1.73

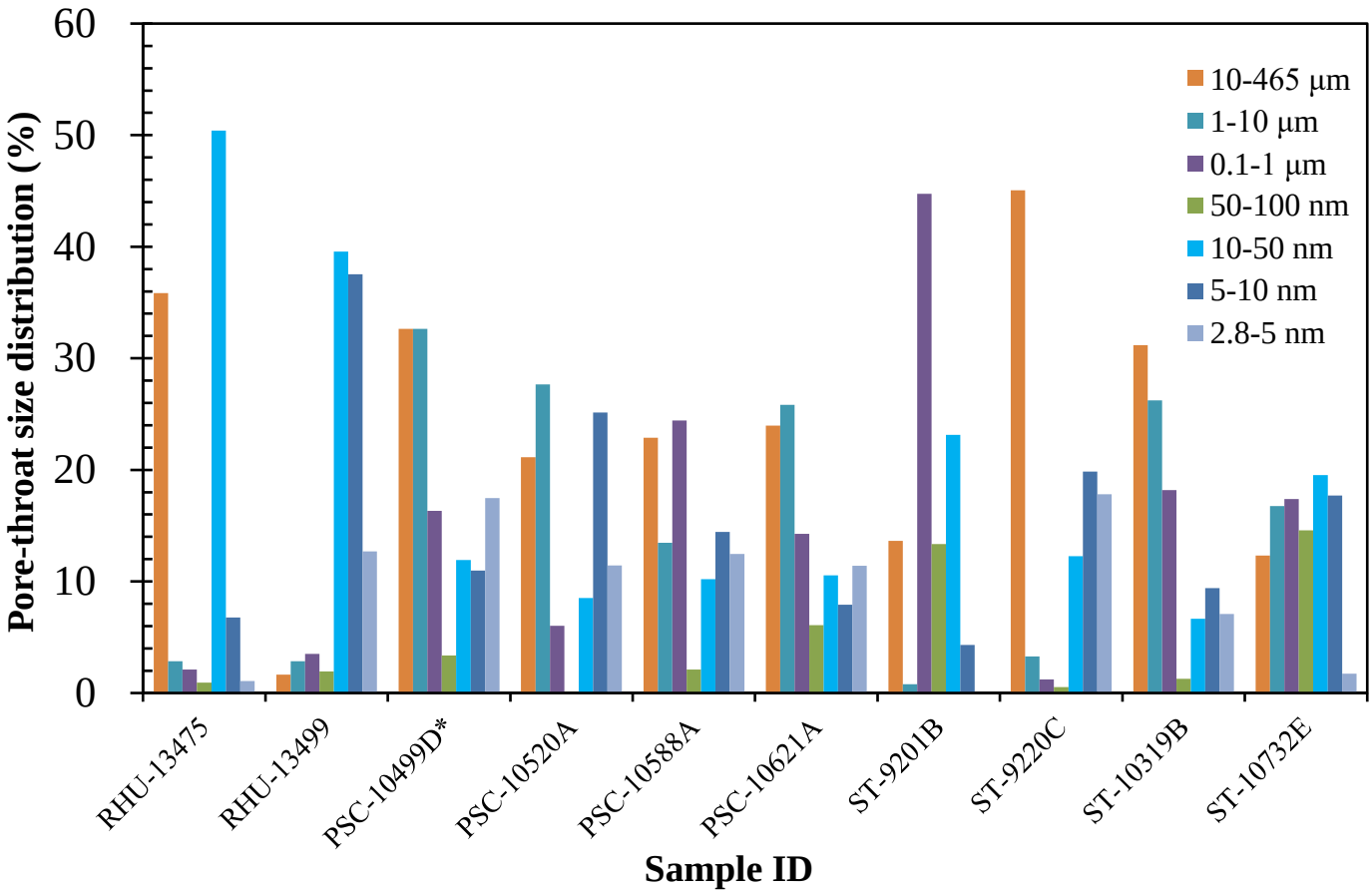

Figure 4.5: Graphic comparison of the pore throat diameter (%) from MICP analyses

4.5 Spontaneous Imbibition

DI water and DT2 were used for spontaneous imbibition in this study. The DT2 is used as a representative for oil. Results from imbibition typically have 2-3 distinct slopes that represent the different stages of imbibition. These distinct slopes are referred to as Stage I, Stage II, and Stage III. Stage I occurs when the sample bottom initially touches the fluid forming a meniscus. This typically occurs in the first few second the experiment begins. Stage II occurs within the first few minutes when the fluid migrates through laminations, microfractures and the sample's edge. Stage III (also known as the connectivity assessment stage) is when the fluid migrates

through the sample matrix. The slope typically remains in Stage III until the samples reaches equilibrium or until the end of the experiment. Occasionally, there can be a fourth slope in Stage IV. The fourth slope typically represents the fluid reaching the top of the sample (Hu et al., 2001). DT2 and DI water imbibition slope figures are shown in Figure 4.8.

Table 7 shows the Stage III slopes for samples that underwent DI water and DT2 imbibition. The connectivity slope qualitatively indicates the pore connectivity of the sample. A slope of ~0.5 indicates a well-connected pore network for the imbibing fluid (Figure 4.6). If the connectivity slope is ~0.25, this indicates that the pore connectivity of the sample is poor (Figure 4.7). For the same samples that underwent both DI water and DT2 imbibition, the slopes for DT2 imbibition were higher than the DI water slopes. The higher DT2 imbibition slopes indicate that the pores of the samples have a better connection to oil-wetting fluids. The results collected from imbibition shows that all samples that underwent DI water imbibition have a low pore connectivity with respect to DI water.

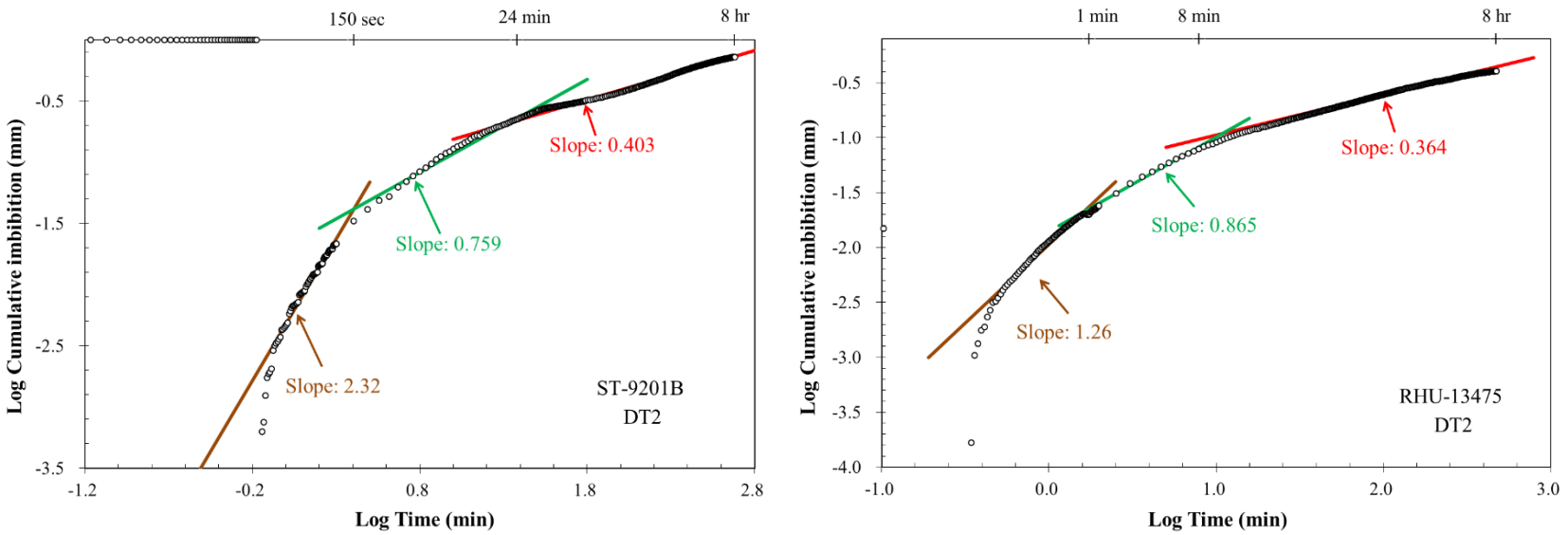

Figure 4.6: DT2 imbibition test of 8-hour run with a connectivity slope of ~0.5 (left). 8-hour DT2 imbibition with a connectivity slope of ~0.25 (right).

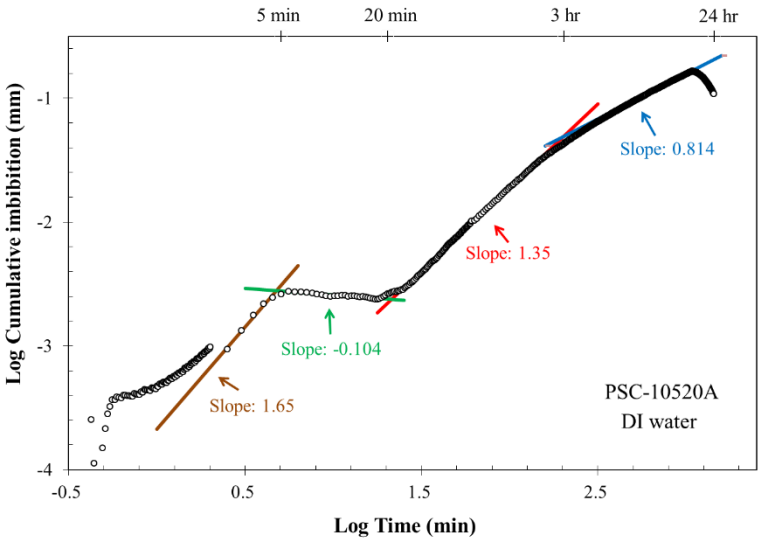

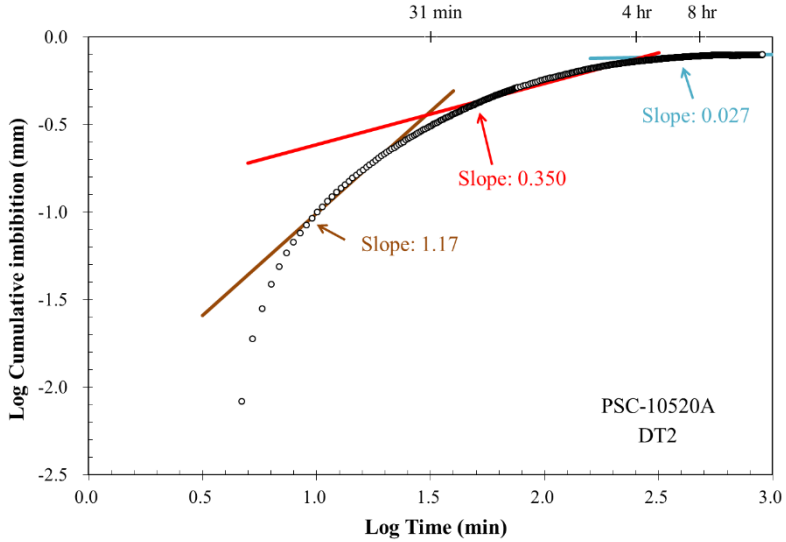

Figure 4.7A: PSC-10520A-WC 24-hour DI water imbibition (left) and PSC-10520A-WC 8-hour DT2 imbibition (right).

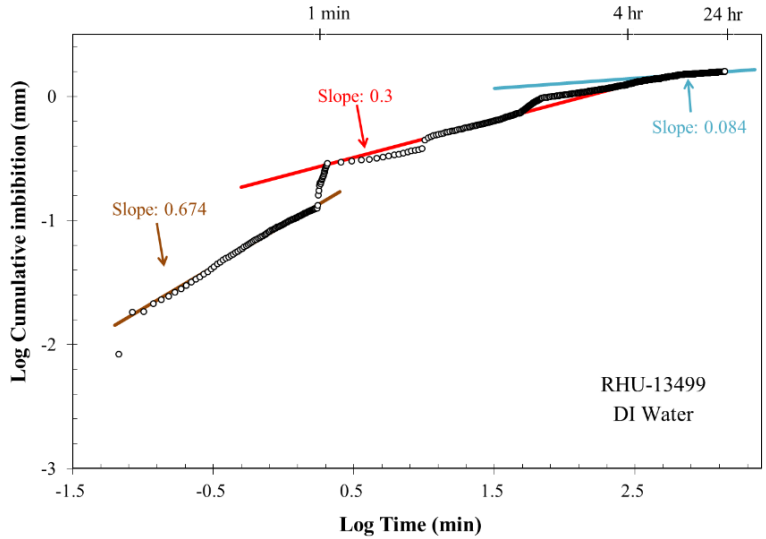

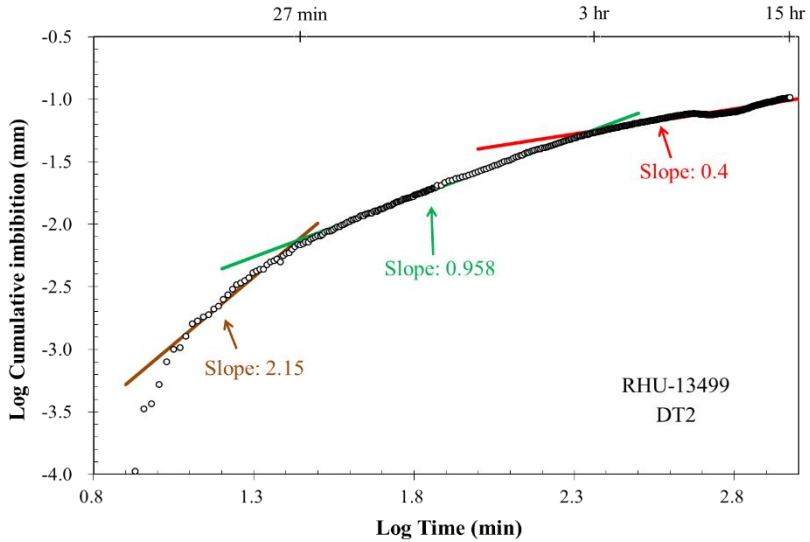

Figure 4.7B: RHU-13499-WC 24-hour DI water imbibition (left) RHU-13499-WC 8-hour DT2 imbibition (right).

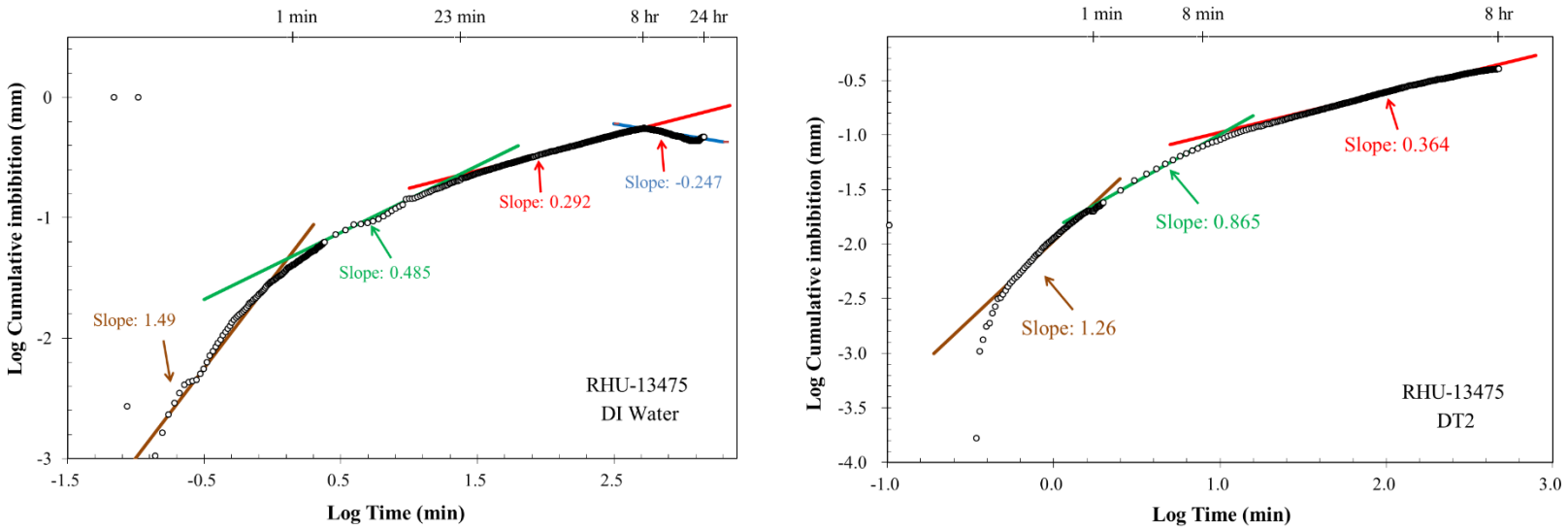

Figure 4.7C: RHU-13475-WC 24-hour DI water imbibition (left) and RHU-13475-WC 8-hour DT2 imbibition (right).

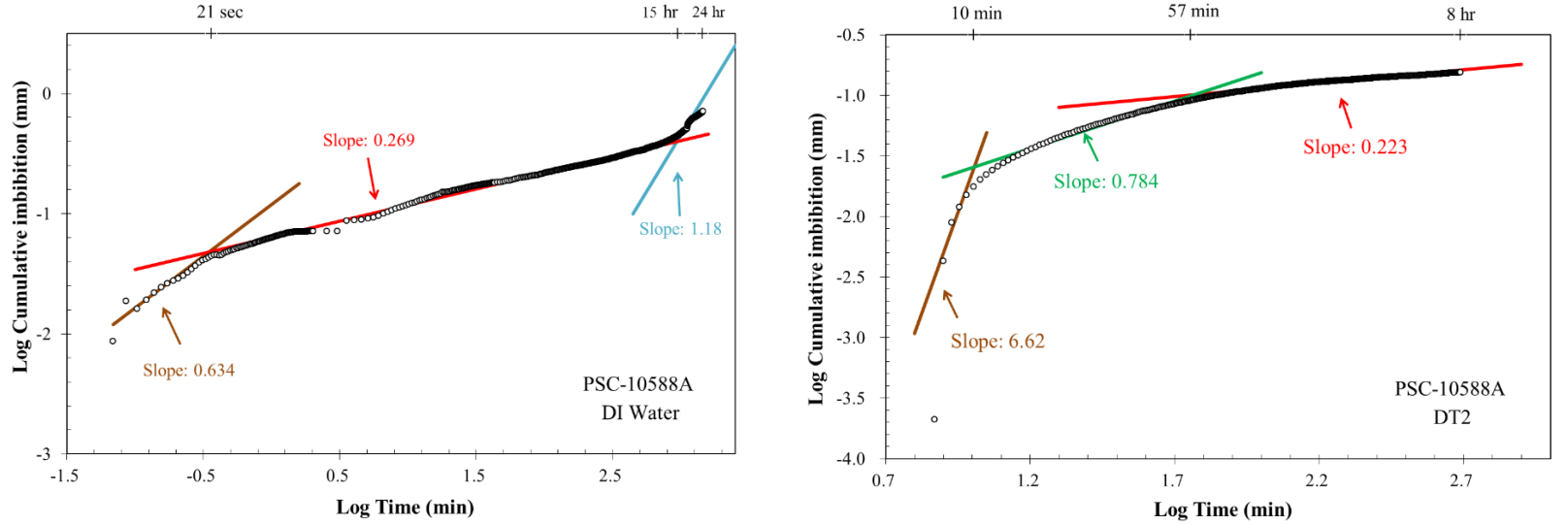

Figure 4.7D: PSC-10588A-WC 24-hour DI water imbibition (left) and PSC-10588A-WC 8-hour DT2 imbibition (right).

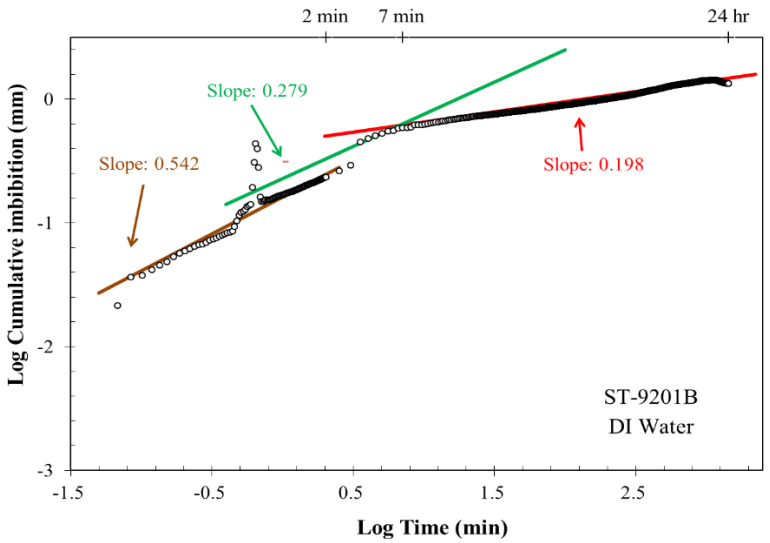

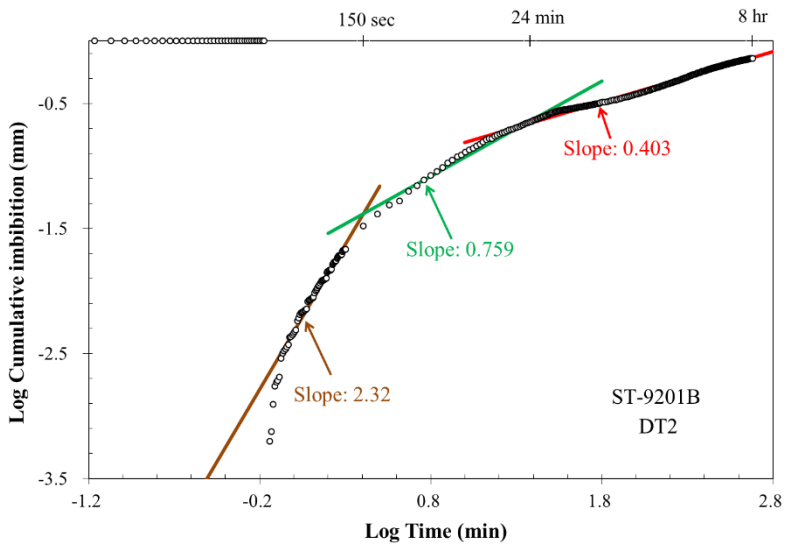

Figure 4.7E: ST-9201B-BS1 24-hour DI water imbibition (left) and ST-9201B-BS1 8-hour DT2 imbibition (right).

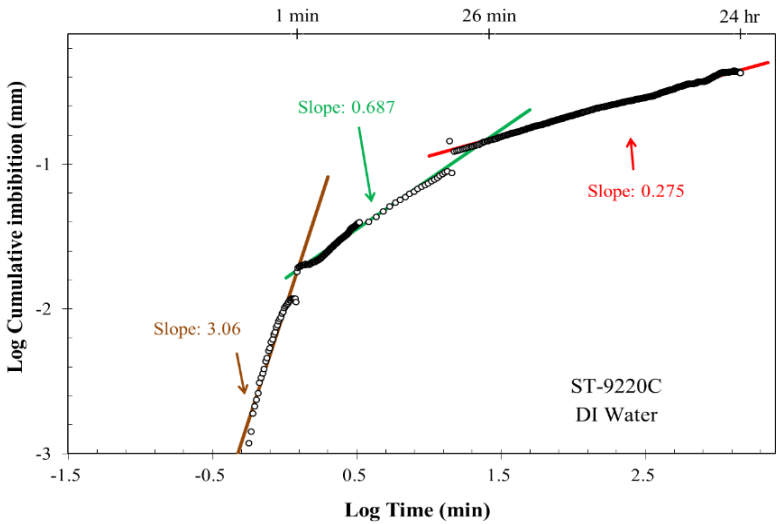

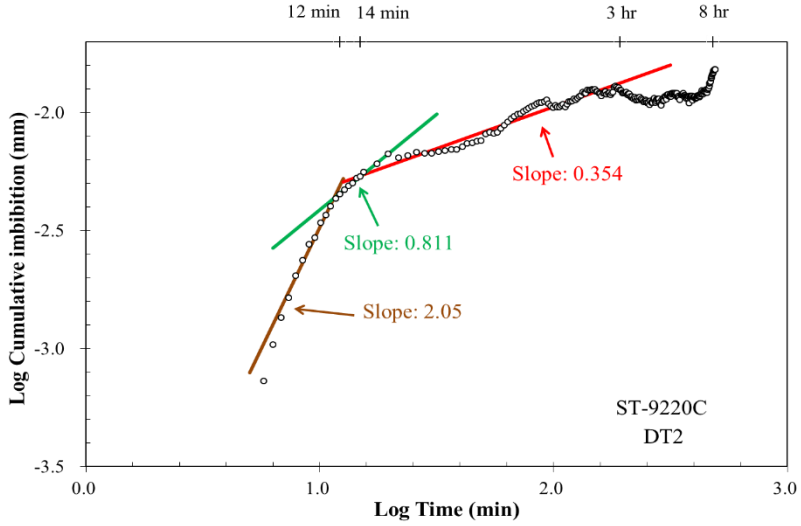

Figure 4.7F: ST-9220-BS1 24-hour DI water imbibition (left) and ST-9220-BS1 8-hour DT2 imbibition (right).

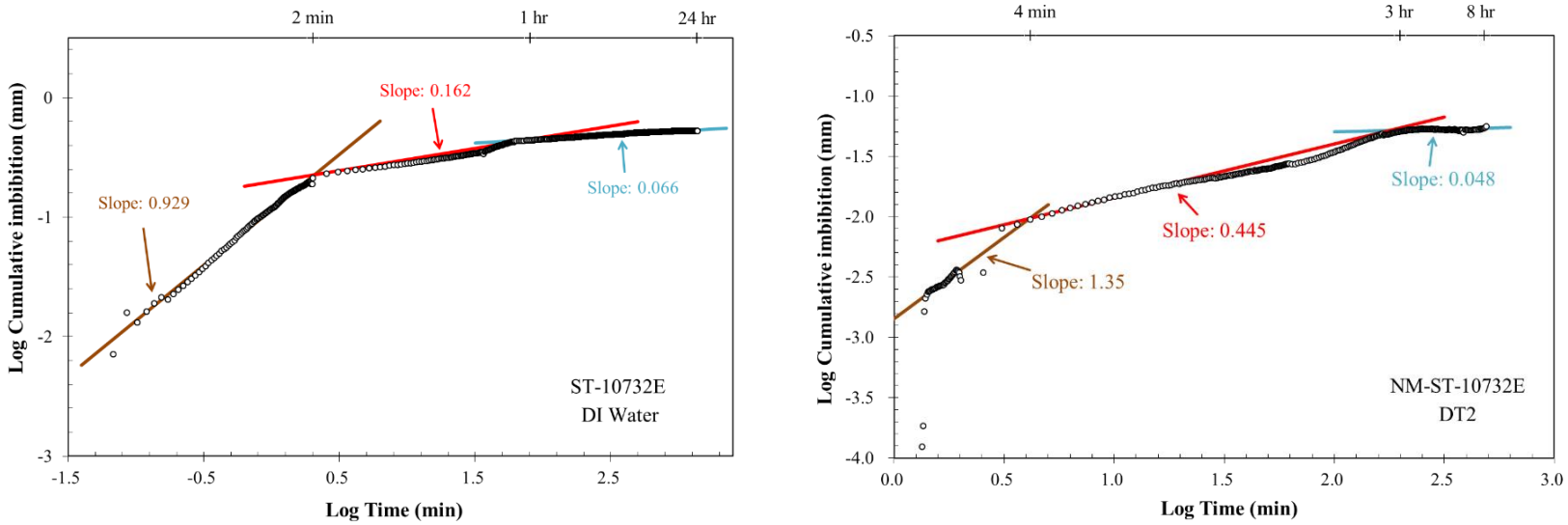

Figure 4.7G: ST-10732E-WC 24-hour DI water imbibition (left) and ST-10732E-WC 8-hour DT2 imbibition (right).

Table 7: Compilation of imbibition results.

Sample ID	Fluid	Connectivity Slope
RHU-13475-WC	DI water	0.292
	DT2	0.364
RHU-13499-WC	DI water	0.300
	DT2	0.400
PSC-10520A-WC	DI water	1.352
	DT2	0.350
PSC-10588A-WC	DI water	0.269
	DT2	0.223
ST-9201B-BS1	DI water	0.181
	DT2	0.403
ST-9220C-BS1	DI water	0.275
	DT2	0.354
ST-10732E-WC	DI water	0.162
	DT2	0.445

4.6 Production

Well data was very limited, and no well logs were available. Red Hills Unit No. 1 is the only well with production data in the NM OCD and Drilling Info database. Peoples Security Co. Well No. 3 and State No. 1 has no data related to production. Peoples Security Co. Well No. 3 was plugged on December 29, 2004 (State of New Mexico OCD, 2019). According to the New Mexico OCD website, State No. 1 is a dry well with no production, and transitioned into a salt disposal well before being plugged in 2008.

The Red Hill Unit No. 1 well has production data dating back to December 1992 (Figure 4.8). From 1992 to 2006, the Red Hill Unit No. 1 well was producing oil and gas. In 2007, the well stopped producing oil; from 2008 until present, the well has only been producing gas.

Table 8: Well details from the New Mexico Oil Conservation Division and Drilling Info.

Well Name	Total Vertical Depth (ft)	Cumulative Oil (bbls)	Status
Red Hills Unit No. 1	21321	438153	Active
Peoples Security Co. Well No. 3	10750	Dry	Inactive, plugged
State No. 1	11040	Dry	Inactive, plugged

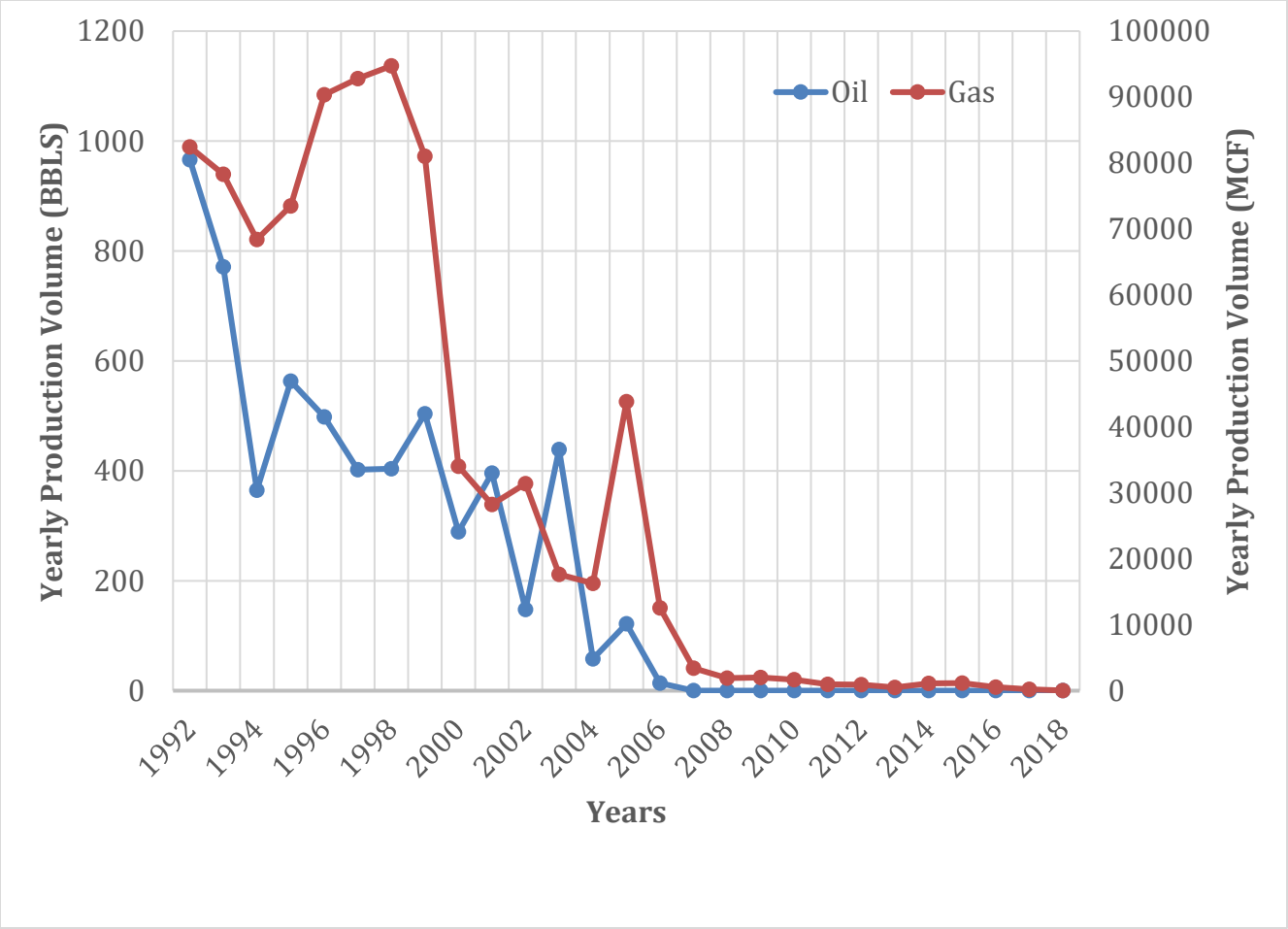

Figure 4.8: Production data for Red Hill Unit No. 1 from 1993-present (NM OCD) (BBLS: barrels of oil; MCF: 1,000 cubic feet of natural gas)

Chapter 5

Discussion

5.1 Mineralogy and Geochemistry

The samples in the Wolfcamp Formation and Bone Spring Formation are predominately quartz or carbonate rich. Most of the samples have a relatively low clay content, except for PSC-10499D-WC. Figure 5.1 and 5.2 compare TOC (%) to the mineral content (%). There is no correlation between the TOC (%) and the mineral content in the Wolfcamp or Bone Spring Formation. In contrast, the lithofacies comparison shows that there is a relationship between TOC (%) and mineral content (%) for the carbonate dominate lithofacies.

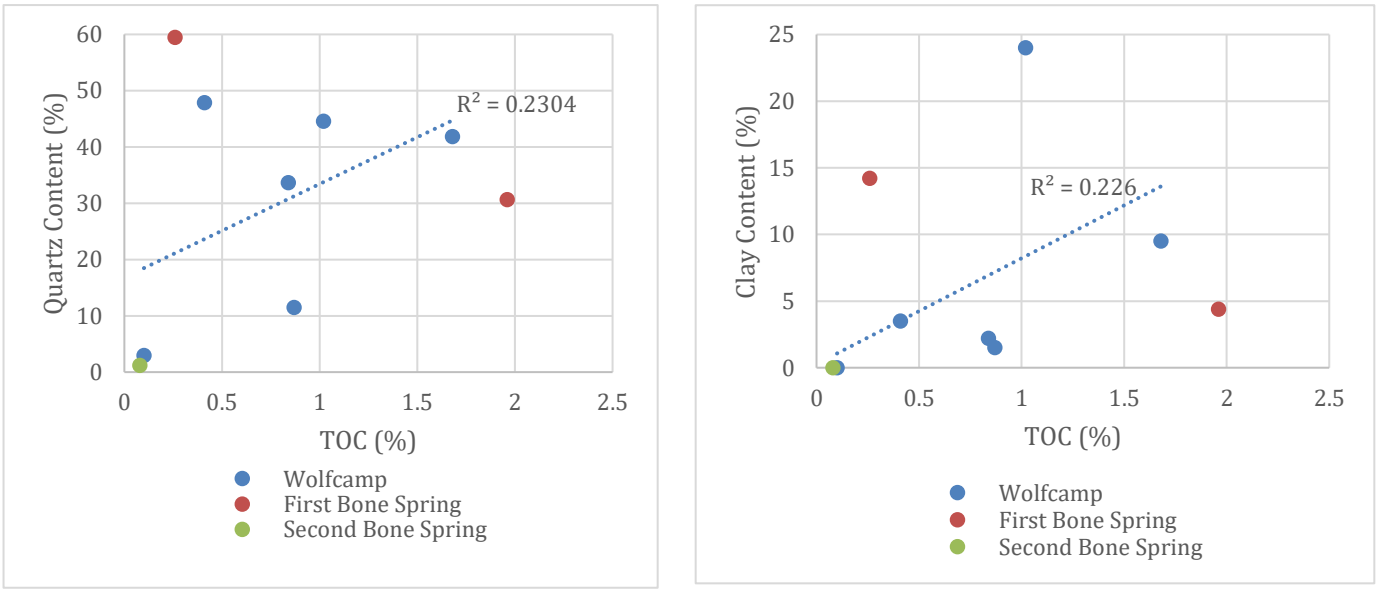

Figure 5.1: Quartz content (%) (left) vs. TOC (%), and clay content (%) vs TOC (%) (right) for samples in the Bone Spring and Wolfcamp Formation.

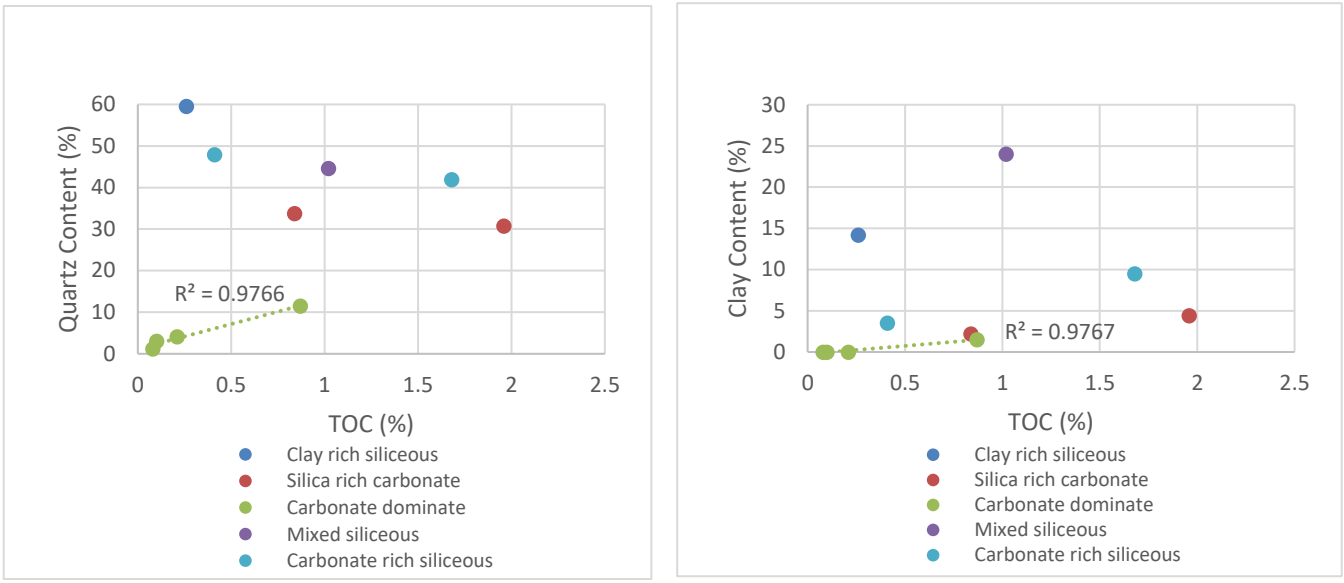

Figure 5.2: Quartz content (%) (left) vs. TOC (%), and clay content (%) vs. TOC (%) (right) for the five lithofacies.

The comparison between S1 and TOC (%) was examined. This comparison includes the oil crossover line proposed by Jarvie (2012). Formations that are above the oil crossover line are expected to be oil productive. Based on Figure 5.3, all the wells are under the oil crossover line, which means all the wells are expected to not produce oil.

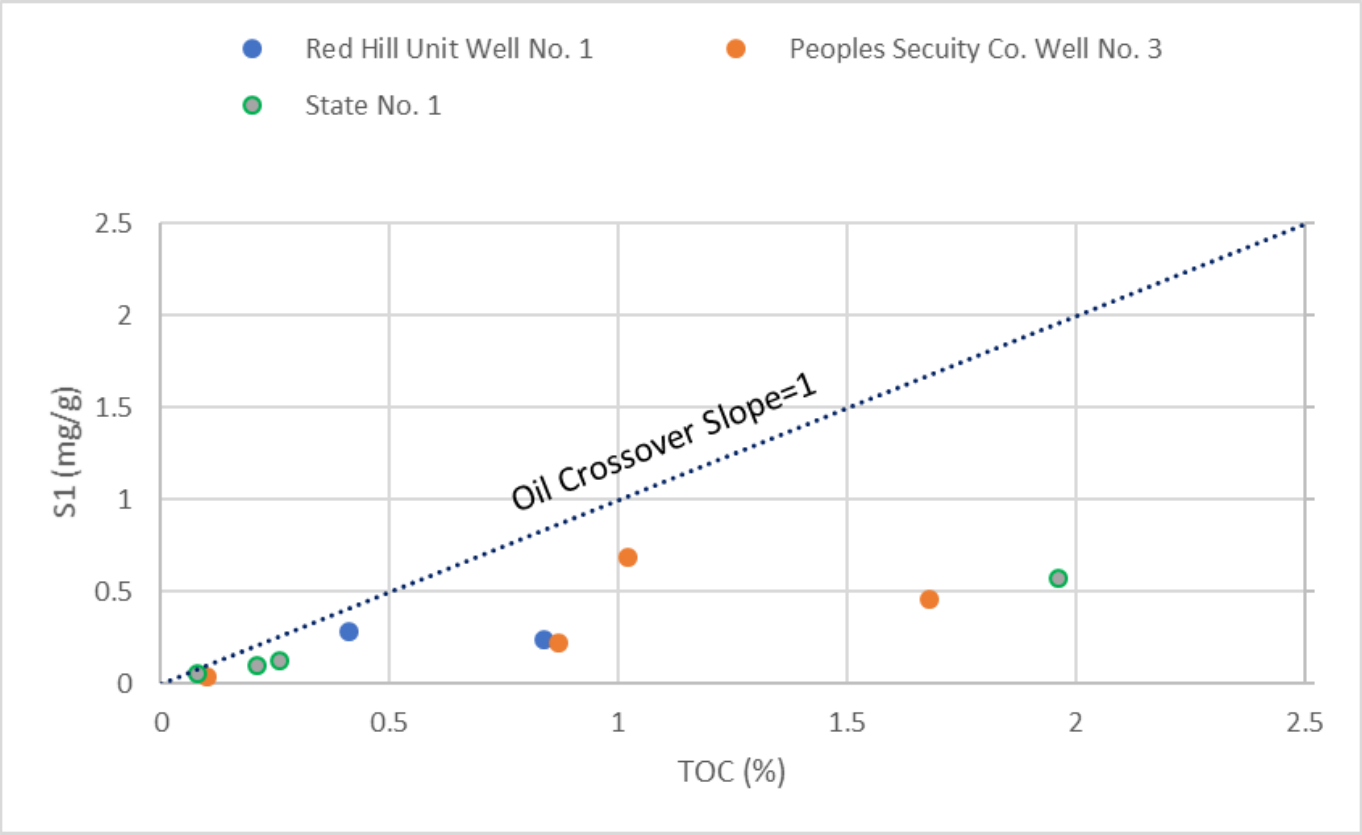

Figure 5.3: Jarvie (2012) oil crossover line of S1 (mg/g) vs. TOC (%).

5.2 Porosity and Permeability

Porosity and permeability are important factors which must be investigated in order to understand the petrophysical properties of a formation. Porosity is difficult to quantify in unconventional shale reservoirs because of the predominance of organic matter (OM) hosted pore spaces. According to Loucks (2009), OM-hosted pores are an important component of the pore system; therefore, a strong correlation between TOC and porosity should be present. However, no relationship between TOC and porosity in the samples was observed (Figure 5.4).

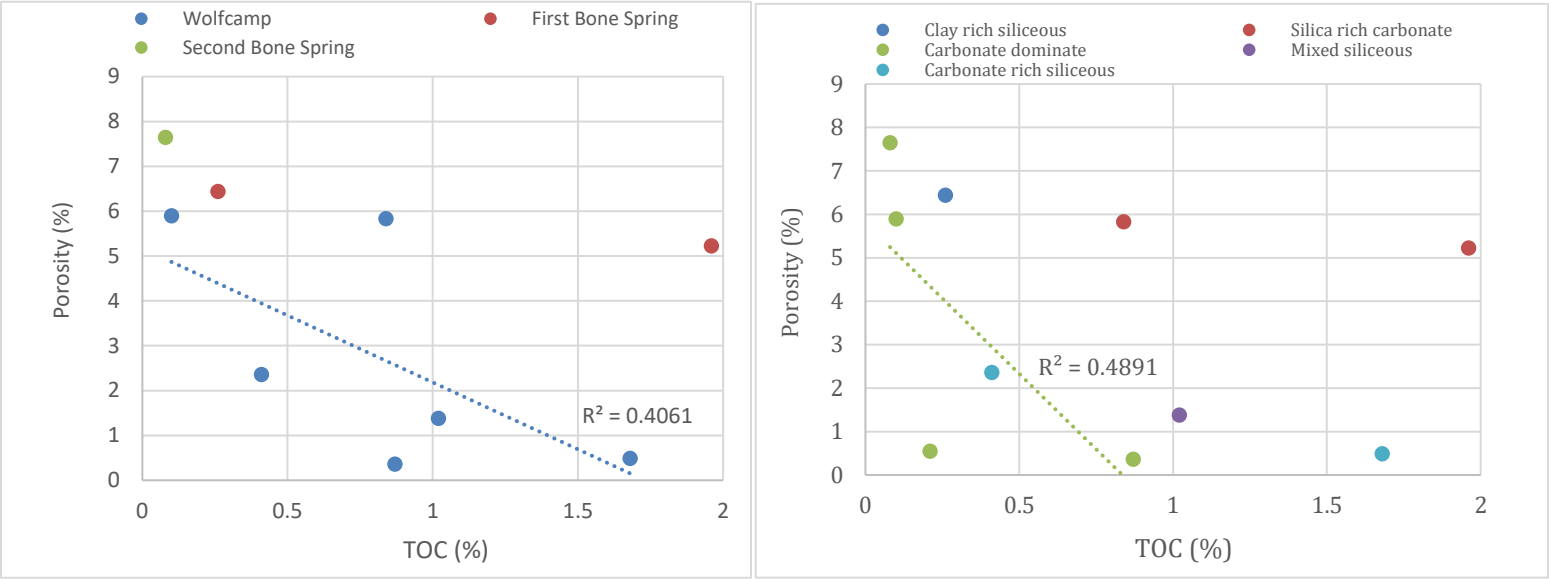

Figure 5.4: Comparison of formations (left) and lithofacies (right) between porosity (%) and TOC (%).

Two different porosity measurement techniques were used in this study. The MICP porosity values for all samples range from 0.49%-7.65%. The vacuum saturation porosity values range from 0.77%-6.33%. The MICP approach shows a slightly higher porosity value in most of the samples in comparison to the vacuum saturation approach. The difference in values can be due to the different matrix properties in the samples. Table 9 shows the porosity range for each formation and its respective lithofacies for MICP and vacuum saturation. The porosity values for a majority of the lithofacies in the Wolfcamp samples are smaller than the porosities observed by Matt Menchaca (2013). M. Menchaca (2013) stated that the Delaware Wolfcamp has a porosity range of 5-9%. The only Wolfcamp lithofacies that falls within this range is the silica-rich carbonate mudstone. Baron and Fritz (2017) found 1-13% porosity in the Second and Third Bone Spring Formation, and New Mexico Tech (2012) found 8-20% porosity in the Bone Spring

Formation. The porosity values from Baron and Fritz (2017) falls within the porosity range found in this study.

Table 9: Porosity ranges from vacuum saturation and MICP.

Formation	Lithofacies	Vacuum saturation (1 cm cube)	MICP (1 cm cube)
		Porosity （%)	Porosity （%)
Wolfcamp	Carbonate dominated lithotype	0.608-3.299	0.360-5.900
	Carbonate-rich siliceous mudstone	0.768-1.421	0.490-2.360
	Mixed Siliceous mudstone	2.830	1.380
	Silica-rich carbonate mudstone	5.381	5.830
First Bone Spring	Clay-rich siliceous mudstone	6.334	6.441
	Silica-rich carbonate mudstone	0.800	5.227
Second Bone Spring	Carbonate dominated lithotype	5.487	7.650

The S1 value determined during pyrolysis analysis is representative of the number of hydrocarbons (mg/g) measured in a sample before thermal pyrolysis. No relationship is observed between S1 and porosity in the samples (Figure 5.5).

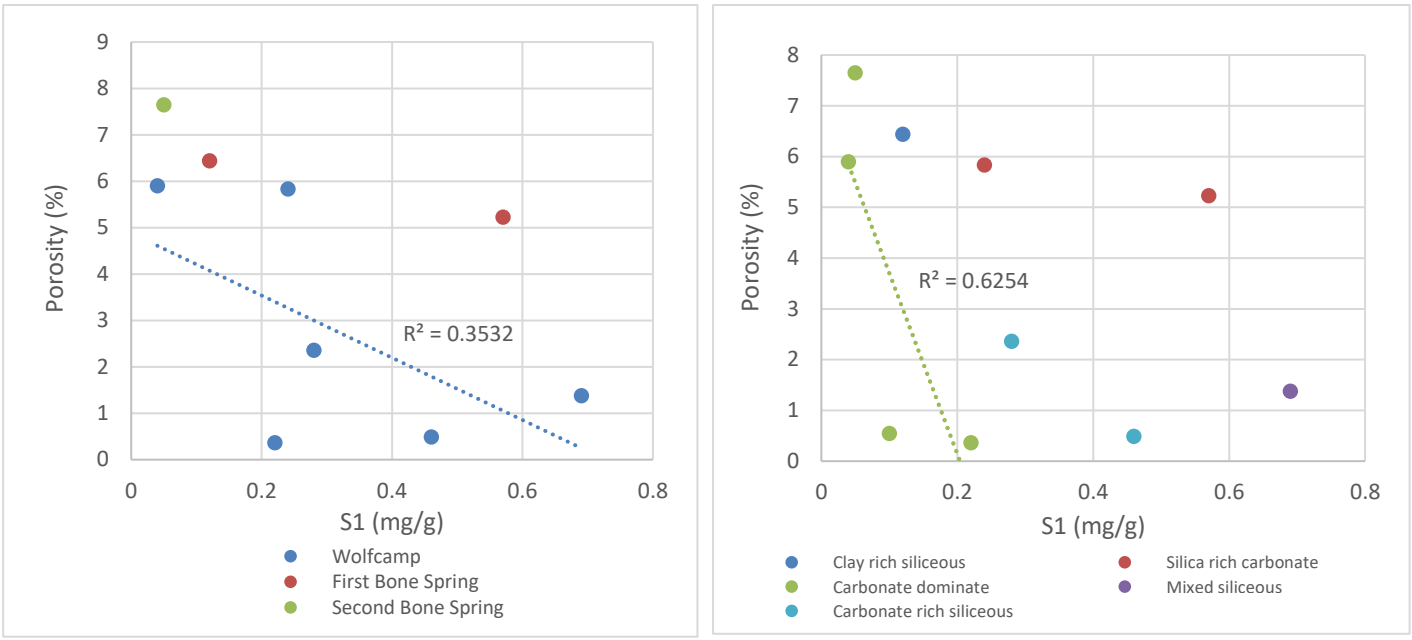

Figure 5.5: Comparison of formations (left) and lithofacies (right) between porosity (%) and S1 (mg/g).

Permeability values for different pore-throat intervals were obtained through MICP analysis. The predominate pore-throat interval permeability for each sample was compared to the porosity obtained through MICP analysis (Table 10). Figure 5.6 (left) shows no correlation between the predominant pore-throat interval permeabilities and the porosity of the samples with respect to their formations. Figure 5.6 (right) compares the predominant pore-throat interval permeabilities and the porosity of the samples with respect to their lithofacies. The lithofacies comparison to permeability and porosity does not show a relationship because there are not enough samples used to display a relationship.

Table 10: The dominate pore-throat interval permeability and porosity used for Figure 5.6.

Sample ID	Porosity (%)	Predominant pore network	
		Pore-throat size (nm)	Permeability (nD)
RHU-13475-WC	5.83	2.8-50	51.52
RHU-13499-WC	2.36	2.8-50	3.57
PSC-10499D-WC	1.38	>100	3.61E+06
PSC-10520A-WC	0.36	>100	3.52E+05
PSC-10588A-WC	5.90	>100	2.32E+08
PSC-10621A-WC	0.49	>100	9.35E+04
ST-9201B-BS1	6.44	>100	1.18E+05
ST-9220C-BS1	5.23	2.8-50	5
ST-10319B-BS2	7.65	>100	1.03E+07
ST-10732E-WC	0.55	>100	5.00E+04

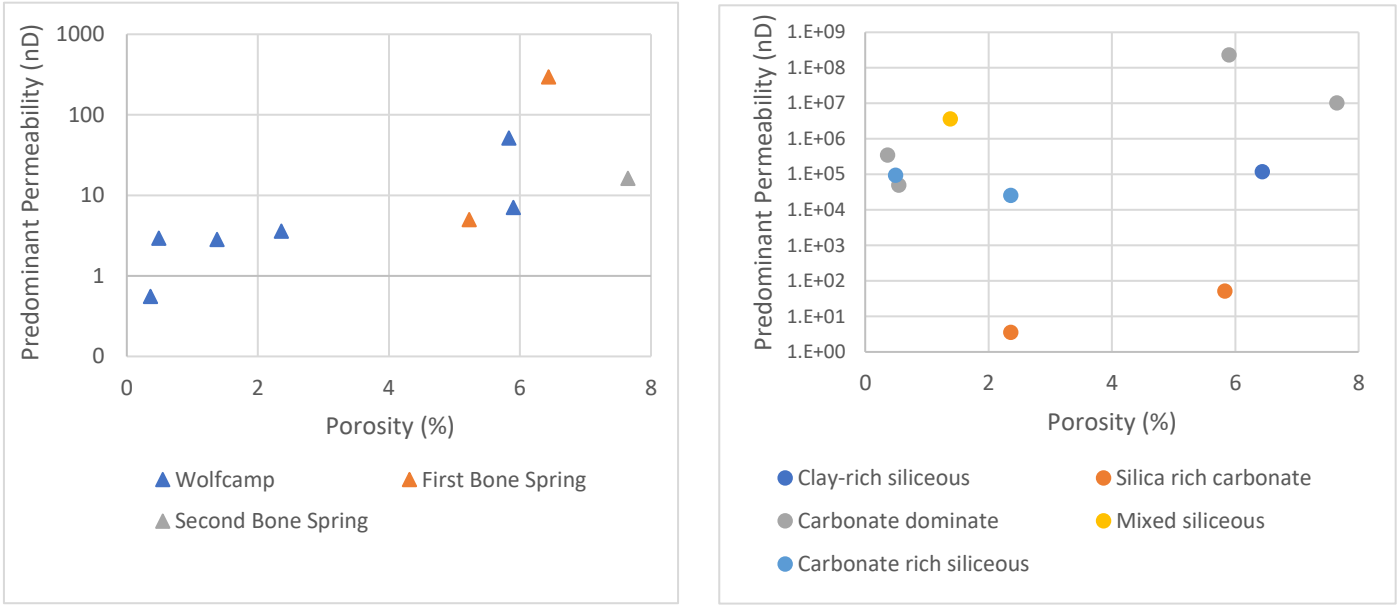

Figure 5.6: Comparison of formations (left) and lithofacies (right) between permeability and porosity.

Permeability and tortuosity significantly vary between the different pore-throat network intervals of 2.8-50 nm and >100 nm pores. When comparing the pore-throat network intervals to the permeability (nD), the >100 nm pore-throat network has permeability values that are a magnitude of 2-9 times larger than the 2.8-50 nm interval. For tortuosity, the 2.8-50 nm values are a magnitude of 1-2 times larger than the >100 nm pore-throat network. Figure 5.7 shows the side by side comparison of the permeability in the two-predominant pore-throat networks. Figure 5.8 shows the comparison of the tortuosity in the two-predominant pore-throat networks. The small geometrical tortuosity values displayed in the >100 nm pore-throats have a dominate amount of microfractures and intergranular pore spaces. Samples that have a predominant pore-throat interval of > 100 nm tend to have good connectivity. Most samples in this study fall in this pore-throat interval. RHU-13499-WC, RHU-13475-WC, and ST-9220C-BS1 are the only samples that fall within the 2.8-50 nm pore-throat interval. These samples should display poor connectivity based on the tortuosity values obtained through MICP.

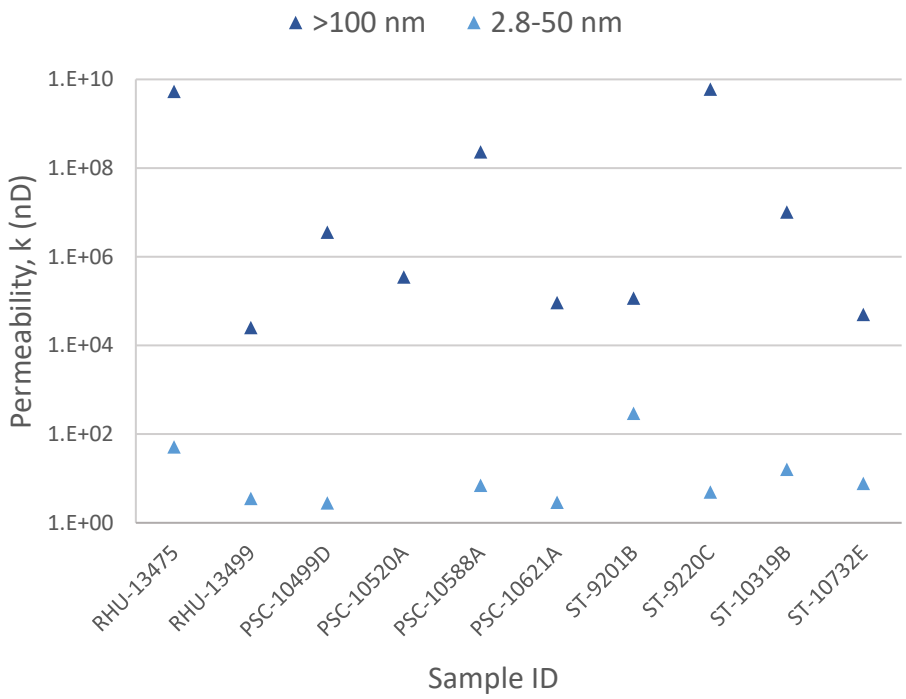

Figure 5.7: Comparison of permeability (nD) in the two pore-throat intervals.

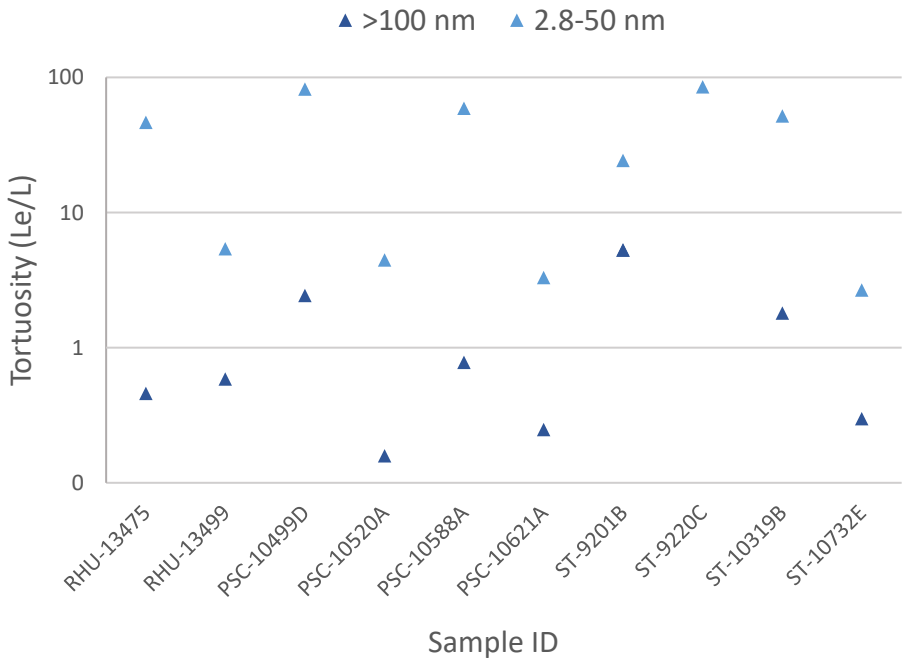

Figure 5.8: Comparison of tortuosity (geometrical) in three pore-throat intervals

5.3 Pore Connectivity

The relationship between the connectivity slope with mineralogy is examined here (Figure 5.9 and Figure 5.10). Samples that have not undergone both DT2 and DI water imbibition will not be taken into consideration for this correlation. Samples RHU-13475-WC, PSC-10588A-WC, and ST-9220C-BS1 have poor connectivity with respect to DI water and DT2. These samples contain a higher percentage of carbonate minerals in comparison to the amount of quartz. Samples ST-9201B-BS1, RHU-13499-WC, and ST-10732E-WC have good pore connectivity with DT2 fluid. The pore connectivity for these samples with DI water is poor. ST-9201B-BS1 and RHU-13499-WC contain more quartz than carbonate minerals. ST-10732E-WC has a large amount of carbonate minerals to the amount of quartz present. Figure 5.9 plots the relationship between DT2 or DI water connectivity to the mineral content for the different lithofacies. The limited number of samples make it difficult to see a relationship between the lithofacies and the two parameters being compared. For the formation comparison, the DT2 connectivity slope and the quartz content shows a relationship (Figure 5.10). As the quartz content increases, the DT2 connectivity slope increases. For DI water connectivity slopes, there is no relationship present with mineral content.

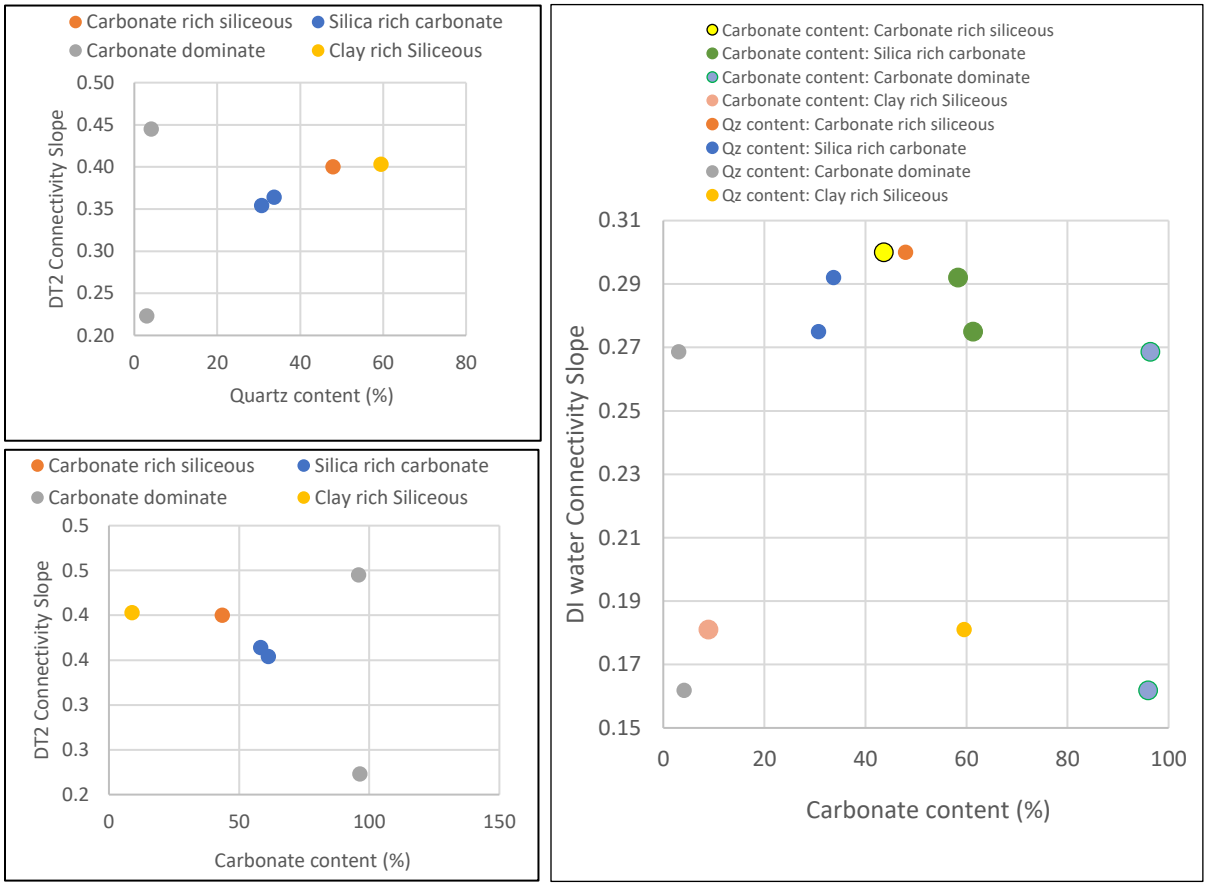

Figure 5.9: Connectivity slopes vs. mineralogy (carbonates and quartz, %) of lithofacies for DT2 (left) and DI water (right).

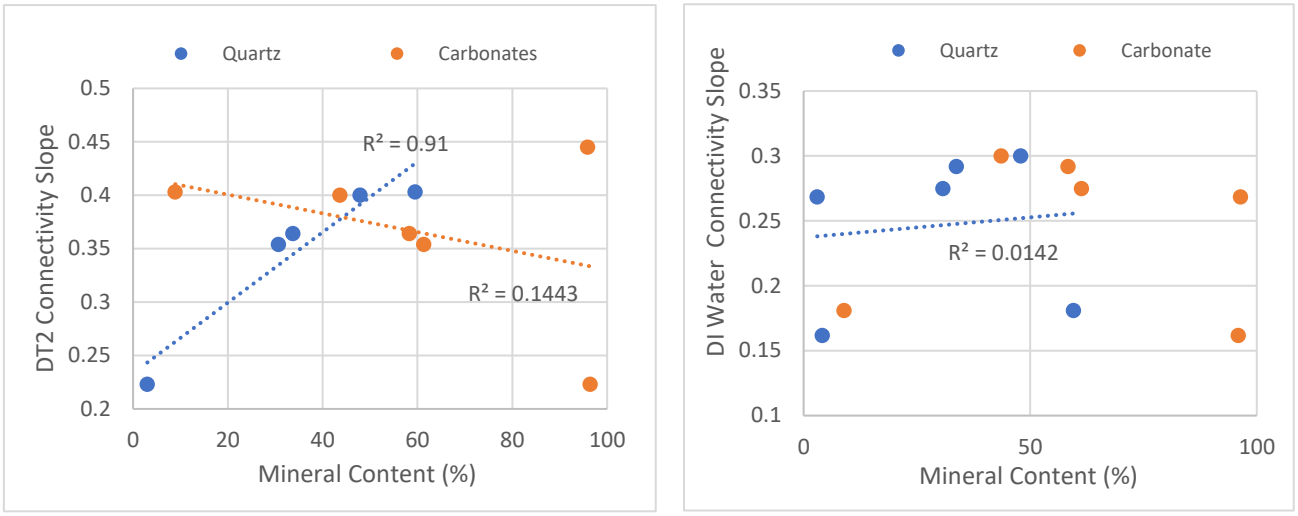

Figure 5.10: Connectivity slopes vs. mineralogy (carbonates and quartz, %) of the Wolfcamp and Bone Spring Formations for DT2 (left) and DI water (right).

Chapter 6

Conclusions and Recommendations

6.1 Conclusions

Samples from the Bone Spring and Wolfcamp Formations in the Delaware Basin were used to explore the petrophysical properties of the formations. The methods used to collect petrophysical data were XRD, pyrolysis, vacuum saturation, liquid displacement, MICP, and spontaneous imbibition.

XRD and geochemistry results show that the samples were dominantly quartz or carbonate rich. Using the sCore lithofacies classification scheme and the XRD data, the lithofacies of the samples were determined. The lithofacies are carbonate dominated lithotype, carbonate-rich siliceous mudstone, mixed siliceous mudstone, silica-rich carbonate mudstone, and clay-rich siliceous mudstone. There is no correlation between mineralogy and the TOC for the formation comparison. For lithofacies comparison, there is a relationship between TOC (%) and mineral content (%) for the carbonate dominate lithofacies. S1 values display no relationship to the porosity (%) in this study.

The results indicate that as a sample's quartz content increases, the DT2 connectivity slope increases. No correlation was found between the DI water connectivity slopes and mineralogy.

MICP tests were conducted once on all samples. The data provides a better understanding of the pore-throat size distribution in each sample. Most samples used in this study have a predominance of pore types associated with microfractures and intergranular pores (> 100nm).. RHU-13499-WC, RHU-13475-WC, and ST-9220C-BS1 have a predominant presence of intragranular pores, organic matter pores, and inter-clay platelet pores (2.8 – 50 nm).

MICP porosity and permeability data were compared in this study. There was no correlation between permeability and porosity for the samples used in this study.

Permeability and tortuosity were found to have a correlation. If permeability was high, the tortuosity was low. Samples with a lower tortuosity are likely to have better connectivity.

6.2 Recommendations

The Bone Spring and Wolfcamp Formations are thick formations that are very anisotropic. A larger sample set is needed to reinforce the findings of this study. Multiple runs for experiments such as vacuum saturation, imbibition and MICP analyses will be needed. This will increase the reliability of the acquired data and can be used to further interpret the different relationships between various characteristics in the formations.

References

Baron, M.V., J. Fritz. 2017. New Method of Defining New Thickness in the Bone Spring Sandstones to Identify Prospective Reservoirs Using Petrophysical Attributes and Stochastic Simulation Techniques in the Delaware Basin, New Mexico.2017 AAPG Annual Convention &Exhibition, Houston, Texas, April 2-5, 2017. Devon Energy Corp., Oklahoma City, Oklahoma. http://www.searchanddiscovery.com/documents/2017/42087baron/ndx_baron.pdf

Bevers, J. 2017. Nano-Petrophysics of the Hybrid Shale-Oil Bone Spring Formation, Lea County, New Mexico. M.S. Thesis, the University of Texas at Arlington, USA.

Curtis M.E., B.J. Cardott, C.H. Sondergeld, C.S. Rai. 2012. The development of organic porosity in the Woodford Shale related to thermal maturity. SPE Annual Technical Conference and Exhibition, Presentation at the Society of Petroleum Engineers, San Antonio, TX, USA, 8-10 October 2012.

Dane, J., C.G. Topp, A.L. Flint, L.E. Flint. 2002. 2.2 Particle Density. DOI: 10.2136/sssabookser5.4.c10

DrillingInfo, 2018. www.drillinginfo.com

Dutton, S., E. Kim, R. Broadhead, C. Breton, W. Raatz, S. Ruppel, and C. Kerans. 2004. Play analysis and digital portfolio of major oil reservoirs in the Permian Basin. Report of Investigations-University of Texas Bureau of Economic Geology, v. 271.

Engle, M.A., F.R. Reyes, M.S. Varonka, W.H. Orem, L. Ma, A.J. Ianno, K.C. Carroll. 2016. Geochemistry of formation waters from the Wolfcamp and “Cline” shales: Insights into brine origin, reservoir connectivity, and fluid flow in the Permian Basin, USA. Chemical Geology, 425, 76-92.

Fairhurst, B., M.L. Hanson, F. Reid, N. Pieracacos. 2012. WolfBone Play Evolution, Southern Delaware Basin: Geologic Concept Modifications That Have Enhanced Economic Success. Search and Discovery Article #10412 (2012).

Gamero-Diaz, H., C.K. Miller, and R. Lewis. sCore: a mineralogy-based classification scheme for organic mudstones. SPE Annual Technical Conference and Exhibition, Presentation at the Society of Petroleum Engineers, New Orleans, LA, USA, September 30, 2013, 10.2118/166284-MS.

Gao, Z., and Q.H. Hu. 2012. Using spontaneous water imbibition to measure the effective permeability of building materials. Special Topics and Reviews in Porous Media – An International Journal, 3 (3): 209-213.

Gao, Z.Y. , Q.H. Hu, and H.C. Liang. 2013. Gas diffusivity in porous media: Determination by mercury intrusion porosmetry and correlation to porosity and permeability. Journal of Porous Media, 16(7): 607-617

Grammer, G.M.. 2013. Characterization of Deep-Water Carbonate Turbidites and Mass Transport Deposits (MTDs) Utilizing High-Resolution Electrical Borehole Image Logs: Late Leonardian (E. Permian) Upper Bone Spring Limestone, Delaware Basin, Southeast New Mexico and West Texas. GCAGS Transactions. 63. 27-65.

Hu, Q.H., P. Persoff, and J.S. Wang. 2001. Laboratory measurement of water imbibition into low-permeability welded tuff. Journal of Hydrology, 242, 64-78.

Hu, Q.H., R. P. Ewing, and H. D. Rowe. 2015. Low nanopore connectivity limits gas production in Barnett formation, Journal of Geophysical Research: Solid Earth, 120, 8073–8087.

Hu, Q.H., R. P. Ewing, and S. Dultz. 2012. Low pore connectivity in natural rock. Journal of Contaminant Hydrology, 133, 76-83.

Hu, Q.H., P. Persoff, and J.S. Wang. 2001. Laboratory measurement of water imbibition into low-permeability welded tuff. Journal of Hydrology, 242, 64-78.

Jarvie, D.M. 2012. Shale resource systems for oil and gas: Part 2—Shale-oil resource systems. Shale reservoirs—Giant Resources for the 21st Century: AAPG Memoir 97, p. 89, doi: DOI:10.1306/13321447M973489.

Keller, G.R., J.M Hills, R. Djeddi. 1980. A Regional Geological and Geophysical Study of the Delaware Basin, New Mexico and West Texas. New Mexico Geological Society Guidebook, 31st Field Conference, Trans-Pecos Region. https://nmgs.nmt.edu/publications/guidebooks/downloads/31/31_p0105_p0111.pdf

Kibria, M.G., Q.H. Hu, H. Liu, Y. Zhang, J. Kang, 2018. Pore structure, wettability, and spontaneous imbibition of Woodford Shale, Permian Basin, West Texas. Marine and Petroleum Geology, 91, 735–748.

Lohr, S.C, E.T. Baruch, P.A. Hall, M.J. Kennedy. 2015. Is organic pore development in gas shales influenced by the primary porosity and structure of thermally immature organic matter? Organic Geochemistry 87: 199-132.

Loucks, R.G., R.M. Reed, S.C. Ruppel and D.M. Jarvie. 2009. Morphology, genesis, and distribution of nanometer-scale pores in siliceous mudstones of the Mississippian Barnett Shale. Journal of Sedimentary Research, 79(11-12): 848-861.

Mann, G. 2017. Petrophysical Properties of the Yeso, Abo and Cisco Formations in the Permian Basin in New Mexico, U.S.A. M.S. Thesis, the University of Texas at Arlington, USA.

Menchaca, M.. 2013. General Overview of Permian Strata of the Delaware Basin and NW Shelf. https://info.drillinginfo.com/general-overview-of-permian-strata-of-the-delaware-basin-and-nw-shelf/

New Mexico Tech. 2012. Play Analysis Part 1. http://infohost.nmt.edu/~petro/faculty/Engler571/Engler471/Appendix-playanalysis-part1.pdf

Quintero, R.P. 2016. Coupled Geochemical and Nano-Petrophysical Study of The Spraberry-Wolfcamp Trend West Texas, U.S.A. M.S. Thesis, University of Texas at Arlington, USA.

Sloss, L.L.. 1988. Sedimentary cover, North American Craton, U.S. v. D-2, Boulder, CO, USA, Geological Society of America.

State Of New Mexico OCD, 2019. https://wwwapps.emnrd.state.nm.us/ocd/ocdpermitting/Data/Wells.aspx

Sutton, L. 2014. The Midland Basin vs. the Delaware Basin- Understanding the Permian. https://info.drillinginfo.com/midland-basin-vs-delaware-basin/

Tokunaga, T.K. and J. Wan. 2001. Surface-zone flow along unsaturated frock fractures. Water Resource Research, 37, No. 2, 287-296.

Tyrrell Jr., W.W. 1966. Wolfcamp Stratigraphy, Western Delaware Basin. Tulsa Geological Society Digest. Symposium on Viola, Fernvale and Sylvan. Vol. 34, 139-140. http://archives.datapages.com/data/tgs/digest/data/034/034001/139_tgs340139a.htm

U.S. Energy Information Administration. 2018. Permian Basin, Wolfcamp Shale Play Geology review. https://www.eia.gov/maps/pdf/PermianBasin_Wolfcamp_EIAReport_Oct2018.pdf

USGS. 2018. USGS Announces Largest Continuous Oil Assessment in Texas and New Mexico. https://www.usgs.gov/news/usgs-announces-largest-continuous-oil-assessment-texas-and-new-mexico

Wang, S., F. Javadpour, and Q.H. Feng. 2016. Confinement correction to mercury intrusion

capillary pressure of shale nanopores. Scientific Reports, 6: 20160, doi: 10.1038/srep20160.

Wood Mackenzie Ltd. 2018. Everything is accelerating in the Permian, including decline rates. https://www.investorvillage.com/uploads/100367/files/TerminalDeclineWoodMac.pdf

Appendix A

Laboratory Methods and Procedures for X-Ray Diffraction Analysis at Shimadzu Institute for Research Technologies

MaximaX XRD-7000: Shimadzu X-ray Diffractometer

Sample Preparation

- Prepare your sample by compacting the sample into the sample holder using a glass slide
- Avoid vertical loading by removing excess sample with the edge of the glass slide
- Attempt to make your sample as flat and homogenous as possible; once this is completed your sample is ready to be analyzed.

Power Operations

- Turn the chiller on by pressing the power button (on the face of the chiller), a green light will illuminate.
    - Allow the chiller to sit for ~20 minutes to adjust to the proper temperature.
- Turn the XRD on by pressing the power button on the left-hand side. The green power button will illuminate on the front panel of the XRD.

XRD Calibration:

- Locate and open the [PCXRD] program on the desktop. The main "XRD-6100/7000" panel will display.
- Click the [Display and Setup] icon, a "door alarm check" window will pop up. Follow the prompt to open and close the XRD door, once complete click "Close". An "IOcon" window will pop up with the message "Now Calibration! If ready OK", Click "OK".
- The XRD is officially calibrated and ready to process your sample.

Setting Analysis Conditions:

- To set the processing conditions go to the "XRD 6100/7000" panel.
- Click on the [Right Gonio Condition] icon to open the [Analysis Condition Edit Program] window
- Click the blue bar under [Measurement Mode: Standard] to open the [Standard Condition Edit] window.
- Most of the settings in the [Standard Condition Edit] window will be preset. Only a few conditions will need to be changed.
- The following general condition settings will work for a wide array of materials.
  It's very important to follow these next steps, double check any settings you change ensuring to follow these guidelines precisely. This will minimize minor mistakes when processing materials and will prevent damage to the detector.
    - Scanning condition: Scan Range (deg) = 2°-70° □ Optional Condition: Check the box [Option Enable]
    - Beta Attachment: Control Mode: Rotation

Rotation Speed (rpm): 6

- Slit Condition: Slit Conditions are preset, and must be verified on the XRD to ensure the proper slit sizes match the settings listed under the Slit Conditions.
  - Checking the Slits:
    - Open the XRD door, on the left side of the XRD is the X-ray tube, the Divergence Slit is attached to the left side of the divergence soller slits.
    - On the right-hand side will be the detector arm which contains a set of Scattering soller slits, the Scattering Slit faces the sample (Left) and the Receiving Slit faces the detector (Right).
    - If they are not the same sizes as what is preset in the [Slit Condition] box change the slit's so they do match.
  - Standard Slit Settings:
    - Divergence Slit: 1.0°
    - Scattering Slit: 1.0°
    - Receiving Slit: 0.3 mm

- Double check your settings and make sure they are correct, if they are click [OK].
- A [File & Sample Condition Edit] window will display; change the [Group name] to match your destination folder name and change [File name] and [Sample Name] to match your sample name, click [New].
  - Later samples can be created by simply changing the file and sample names and clicking [Modify].
- Click [Close] on the [Standard Condition Edit] window.

Starting the XRD Processing:

- Locate and click the [Right Giono Analysis] icon on the [XRD-6100/7000] panel.
- Your current sample name should appear highlighted blue in the upper portion of the [Right Gonio System: AnalysisCondition Edit Program] window. Highlight your sample and click [Append], this adds your sample to the list in the bottom portion of the window labeled [Entry for Analysis], click [Start]. Your sample should appear in the bottom of the [Right Giono Analysis & Spooler Program] window, click [Start] in this window. This officially starts the analysis process.
  - Indicators for Analysis: A clicking sound will come from the XRD when the locking mechanism on sliding door locks. On the face of the XRD a yellow light should illuminate under [X-RAYS ON].
- Leave all software windows open and allow the XRD to process your sample, this should take ~30 minutes.

Completed XRD Processing:

- A complete peak spectrum should appear in the [Right Giono Analysis & Spooler Program] window upon completion.
- The green [Analyzing!] Box should disappear and the yellow [X-RAYS ON] light should turn off.

- If you have more samples to analyze, continue to run your samples in the same manner listed above.

Opening Peak Profile Spectrum:

- Locate and open the icon for the [MDI jade 9] software on the Desktop.
- Under [file], click [Read], locate the folder [xddat] under [favorites]. Locate the folder where your samples are saved.
- In your folder, each sample should have a [.RAW] file, use this file to open your selected spectrum in the [Jade 9] software.

Identifying Minerals in Peak Spectrum:

It's important to have an educated background on the sample you're analyzing. Knowledge regarding the bulk composition and what you're searching for will greatly reduce the amount of time spent IDing the various peaks in the spectrum.

- Locate the [Find Peaks] icon on the main tool bar next to the [Floppy Disk/Save] icon, this will identify and mark any statistically significant peaks within the spectrum
- Choose a mineral database: At the top of the panel to the right of the spectrum window, there will be a drop-down menu choose the [RDB-Minerals] as the database. The RDB-Mineral database should be predominately used to identify most minerals in your spectra.
    - If you cannot find a mineral in the RDB-Minerals database change to the [PDF+4 Minerals] database library, but be sure to change back to the RDB database once the mineral is located.
- Begin searching for minerals based on your pre-existing knowledge regarding the sample. When you identify minerals that fit your peak spectrum hit [Enter] on the keyboard, this process will add the minerals to a compiled list of those minerals which you identified in the spectrum.
- Once you have exhausted your initial hypothetical list of minerals, a helpful tool to use is the [Line Based Search/Match]. Go to the main tool bar and locate [Identify] and select the [Line Based Search] option.
    - This tool will compile a list of minerals by searching a selected PDF database for entries with peaks which are statistical matches for the peaks identified within your spectrum.
    - Settings:
        - [Two-Theta Error Window] max setting should be no more than 0.24%
        - [Top Hits to List] max setting 80
    - Set the parameters and click the blue [Play] icon next to the [X] to run the search and generate a list of possible phases that might fit your spectra. *Note: the line based search should not be used as a primary way to identify the bulk mineral mode of the sample as the software is not consistent when generating phases and will possibly leave out important phases for the spectrum*.

Model Analysis:

- Once all minerals have been ID'd, check that they have been added to the mineral list by pushing [Enter] on the keyboard.

- Click the [%] icon next to the drop-down mineral list located on the toolbar in the middle of the window to begin modal analysis.
    - An overlay will appear with different chart configurations of the modal results, to change the configurations of the chart use the drop-down menu in the chart window.
- To view the modal analysis in text format: locate and click the […] icon near the [%] icon. This will list the minerals by name, chemical formula, and the normalized weight percent for each mineral. It will also state if the mineral is a [major], [minor], [trace], or [absent] component in the sample.
- If you would like to remove a mineral from your mineral list at any time, highlight the mineral and press [Delete] on the keyboard. [Absent] phases should be removed from the list by this method.

Analysis Check with Pattern Deconvolution:

- A key indication that the peak spectrum has been fully fitted and identified is by using the [Pattern Deconvolution] tool which automatically runs with the modal analysis.
    - The pattern deconvolution tool will generate a red overlay spectrum on top of the original white spectrum.
    - This process is generating a [Best Fit Profile] composed of the selected mineral standards from the [Mineral PDF database library] with your sample spectrum.
    - If all minerals have been properly identified, then the red deconvolution overlay will match the peak spectra for each peak. If there are peaks that don't have the red deconvolution overlay then those peaks have not been identified.
- Continue processing your spectrum until your original spectra and the deconvolution spectra match.

Saving Data:

To save your data,

- Go to [file] and [Save], save your data under [Current work as *.SAV]. This will save all analysis as a separate file.

Appendix B

Laboratory Methods and Procedures for TOC and Pyrolysis Analysis at GeoMark Research, LLC.

Procedures – GeoMark Research, LLC.

1. Sample Requirements for a Typical Geochemical Program

For geochemical analysis a teaspoon (ca. 10 g.) of sample material is needed when TOC, Rock-Eval, vitrinite reflectance and residual hydrocarbon fluid fingerprinting is to be completed. If possible, a tablespoon is preferred. However, it is possible to complete a detailed program with even less sample, although there is dependency on the sample characteristics (e.g., organic richness, abundance of vitrinite, amount of staining). Sample prep includes grinding the sample with mortar and pestle until it passes through a 60-mesh sieve.

2. Total Organic Carbon (TOC) – LECO C230 instrument

Leco TOC analysis requires decarbonation of the rock sample by treatment with hydrochloric acid (HCl). This is done by treating the samples with Concentrated HCl for at least two hours. The samples are then rinsed with water and flushed through a filtration apparatus to remove the acid. The filter is then removed, placed into a LECO crucible and dried in a low temperature oven (110 C) for a minimum of 4 hours. Samples may also be weighed after this process in order to obtain carbonate% based on weight loss.

The LECO C230 instrument is calibrated with standards having known carbon contents. This is completed by combustion of these standards by heating to 1200°C in the presence of oxygen. Both carbon monoxide and carbon dioxide are generated, and the carbon monoxide is converted to carbon dioxide by a catalyst. The carbon dioxide is measured by an IR cell. Combustion of unknowns is then completed and the response of unknowns per mass unit is compared to that of the calibration standard, thereby the TOC is determined.

Standards are analyzed as unknowns every 10 samples to check the variation and calibration of the analysis. Random and selected reruns are done to verify the data. The acceptable standard deviation for TOC is 3% variation from established value.

3. Rock Eval / HAWK Pyrolysis

Approximately 100 mg of washed, ground (60 mesh) whole rock sample is analyzed in the Rock-Eval or HAWK instrument. Organic rich samples are analyzed at reduced weights whenever the S2 value exceeds 40.0 mg/g or TOC exceeds 7-8%. Samples must be re-analyzed at lower weights when these values are obtained at 100 mg.

RE-II Operating Conditions

S1: 300oC for 3 minutes
S2: 300oC to 550oC at 25oC/min;
hold at 550oC for 1 minute
S3: trapped between 300 to 390o

RE-VI Operating Conditions

S1: 300oC for 3 minutes
S2: 300oC to 650oC at 25oC/min;
hold at 650oC for 0 minute
S3: measured between 300 to 400o

HAWK Operating Conditions

S1: 300oC for 3 minutes
S2: 300oC to 650oC at 25oC/min;
hold at 650oC for 0 minute
S3: measured between 300 to 400o

Measurements from Rock-Eval are:

S1: free oil content (mg HC/g rock)
S2: remaining generation potential (mg HC/g rock)
Tmax: temperature at maximum evolution of S2 hydrocarbons (oC)
S3: organic carbon dioxide yield (mg CO2/ g rock)

Several useful ratios are also utilized from Rock-Eval and TOC data. These are:

Hydrogen Index (HI): S2/TOC x 100 (in mg HC/g TOC)
Oxygen Index (OI): S3/TOC x 100 (in mg CO2/g TOC)
Normalized Oil Content: S1/TOC x 100 (in mg HC/g TOC)
S2/S3:
Production Index (PI): S1/ (S1+S2)

Instrument calibration is achieved using a rock standard. Its values were determined from a calibration curve to pure hydrocarbons of varying concentrations. This standard is analyzed every 10 samples as an unknown to check the instrument calibration. If the analysis of the standard ran as an unknown does not meet specifications, those preceding data are rejected, the instrument recalibrated, and the samples analyzed again. However, normal variations in the standard are used to adjust any variation in the calibration response. The standard deviation is considered acceptable under the following guidelines:

Tmax: □ 2oC
S1: 10% variation from established value
S2: 10% variation from established value
S3: 20% variation from established value

Analytical data are checked selectively and randomly. Selected and random checks are completed on approximately 10% of the samples. A standard is analyzed as an unknown every 10 samples.

4. Turnaround Time:
The standard turnaround time for sample orders over the past 12 months is approximately 2 to 3 weeks, depending on number of samples in the order.